University of Waterloo

Faculty of Engineering

# Topological optimization in additive manufacturing of rocket engines

Submitted in fulfillment of research requirement for ME739

Stefan Martin, Trevor McCourt
March 16th, 2020

# Contents

# List of Figures

# 1. Abstract

For high-power rocketry applications there are few materials which can handle the sustained heat and pressure within the combustion chamber and nozzle. With some engines reaching gas temperatures in excess of 3300C [1] and pressures on the order of 300 atmospheres [15] exotic cooling strategies must be considered. Metal additive processes have recently become feasible alternatives to conventional manufacturing processes when it comes to the design of rocket motors due to the specific topological and structural advantages that additive processes provide. This is most clearly seen in areas of weight reduction, generative design methods, and intricate internal geometries which would be otherwise impossible. To explore this topic, we will conduct a review of the current state of the art in literature for topology optimization in addition to performing design optimization of a real printed rocket nozzle.

# 2. Introduction

## 2.1 Background

Major rocket companies such as SpaceX [5, 4] have switched to using additively manufactured components in the high heat and high-pressure areas of their liquid rocket engines. Selective laser melting (SLM) has become increasingly popular in this space in recent years. The reasons for this are straightforward; traditional manufacturing methods for these engine components are extremely costly and complex. Most modern rocket engines need to be actively cooled by passing chilled fuel over hot components to absorb the heat which would otherwise melt the materials in use. Conventional processes for achieving this include tube bonding[16] and channel milling with hot isostatic pressure bonding of a separate liner to an outer shell to form a pressure tight seal[16]. This complexity is well demonstrated in the space shuttle main engine (SSME) which requires 1080 separately bonded tubes [1] to carry the coolant around the engine bell, a laborious and error-prone process.

**Figure 2.1:** Space Shuttle Main Engine, (RS-25) showing tube structure. From [1]

Compared to the traditional methods, the advantages of SLM are severalfold. Specifically, additive processes allow for construction of monolithic components to perform multiple functions which greatly simplifies assembly[17]. But perhaps the most important feature is the ability to print highly complex geometries not accessible to other manufacturing methods. Internal features, lattice structures, microchannels and topologically optimized features are of special interest in rockets due to the focus on weight reduction and providing integral fluid paths wherever possible[16]. In their paper, Gradl et al. state that SLM processes provide "fabrication options not previously possible with other manufacturing techniques including complex internal and integral design features"[17]

## 2.2 Current State of the Art

Research into the area of additively manufactured (AM) rocket engines has largely been completed at NASA. Gradl et al. review NASA's progress in the area of AM rocket components up to 2018 [3, 18]. This long article will be summarized here. The focus at NASA seems to be on the additive manufacturing of 4 specific parts of the rocket engine: the fuel injector, combustion chamber, nozzle, and spark igniter. These are shown amongst a rocket engine schematic in figure 2.2.

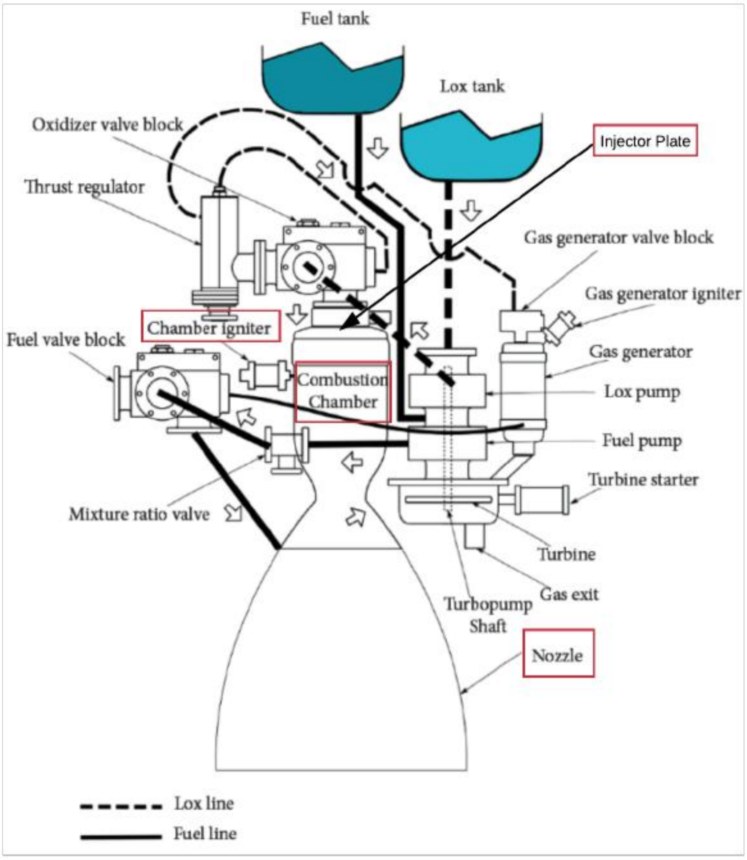

**Figure 2.2:** Schematic of Brazillian L75 rocket engine showing location of relevant components. Figure adapted from [2].

The purpose of the injector in liquid and hybrid rocket engines is to spray the fuel and oxidiser into the combustion chamber, such that the flow of the two fluids combines as droplets, increasing ease of combustion [19]. Generally, injectors are plates with strategically placed small holes that atomize the fuel into the combustion chamber in a desired spray pattern. Conventionally fabricated injectors typically have many parts, which are then assembled using techniques such as brazing and welding. Additive manufacturing allows injectors to be fabricated monolithically, typically using SLM. Most of the NASA injectors have been made out of Inconel 625 due to its excellent corrosion resistance. Small feature resolution, surface roughness and removing residual powder from the injector channels are the current problems being addressed in the additive manufacturing of injectors. Figure 2.3 A shows an example of an AM injector.

Combustion of the fuel and oxidiser takes place in the combustion chamber (CC). The CC gets extremely hot, generally requiring active cooling. This explains why NASA has pursued the additive manufacturing of this part in particular due to the opportunities for creating internal features using AM techniques. NASA combustion chambers are generally regeneratively cooled, meaning the oxidiser is used as coolant before being burned via running it through channels in the chamber wall. Entire combustion chambers have been fabricated out of various Inconel and copper alloys, along with copper combustion chamber liners indented to be used as a replaceable part in a reusable engine. These chambers are almost always fabricated using SLM [17], although NASA has experimented with directed energy deposition (DED) combined with heavy post-machining. These AM combustion chambers simplify fabrication significantly. However, similar to the case of injectors, surface roughness leads to a greater pressure drop that desired in the cooling channels. Figure 2.3 B and C show examples of copper and Inconel combustion chambers, respectively.

At the scale of NASA, additive nozzle manufacturing is uniquely challenging, since current SLM build volumes are much smaller than the nozzles used on large rocket engines. Several small nozzles have been fabricated using SLM, cooled either regeneratively, via radiation, or by transpiration cooling. This last method is unique where a small amount of fluid is allowed to pass through the nozzle wall onto the hot surface which it will then cool via both conduction and evaporation modes. All of these small SLM nozzles were fabricated out of Inconel and successfully hot-fire tested. An example is given in figure 2.3 D. NASA has also experimented with using other additive process for larger (>1000 lbf thrust) nozzles. A wire-deposition based process has been used in a hybrid conventional-additive nozzle, in which the coolant channels were conventionally manufactured, and then lined using a stainless steel wire deposition process to form a pressure tight seal. This allows for larger nozzles with smoother coolant channels for less coolant pressure drop. This nozzle is shown in figure 2.3 E. A single-piece nozzle was also fabricated out of Inconel using a powder DED process [20]. This nozzle had internal coolant channels for regenerative cooling and performed better in terms of pressure drop than the wire deposition based nozzle. This nozzle is shown in figure 2.3 F.

Spark igniters are another component that resides in the combustion chamber with significant AM interest. The spark igniter delivers an electrical spark to initiate combustion. It experiences very high heat, and is classically fabricated out of copper and nickel. Inconel additive manufacturing techniques combined with CNC finishing have reduced the time required to fabricate this part from months to days, although additive manufactured igniters typically need to be actively cooled due Inconel's low thermal conductivity. An example of such a spark igniter is given in figure 2.3 G.

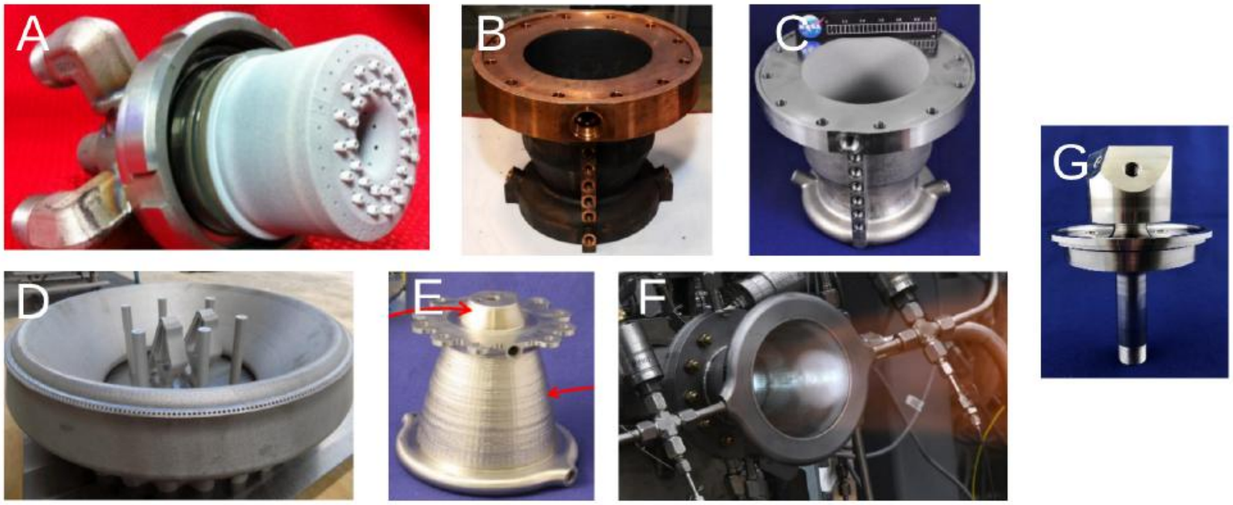

**Figure 2.3:** Various NASA engine components made with AM techniques. Individual images from [3].

SpaceX is another leader in the field of AM rocket engines. However, information on work completed at SpaceX is limited due to lack of research publications. Most comes from ad-hoc social media posts by the SpaceX CEO Elon Musk. They have reported on one main engine that uses additively manufactured components: the SuperDraco.

The SuperDraco is a relatively small engine designed for use as the launch abort system for the Dragon V2 capsule. The engine operates on the hypergolic UDMH and nitrogen tetroxide mixture and produces approximately 16,000lbf (73kN). It is reportedly made out of Inconel using an EOS SLM machine [5]. It is reported to be regeneratively cooled using internal channels. Evidence of this can be seen in figure 2.4 (B).

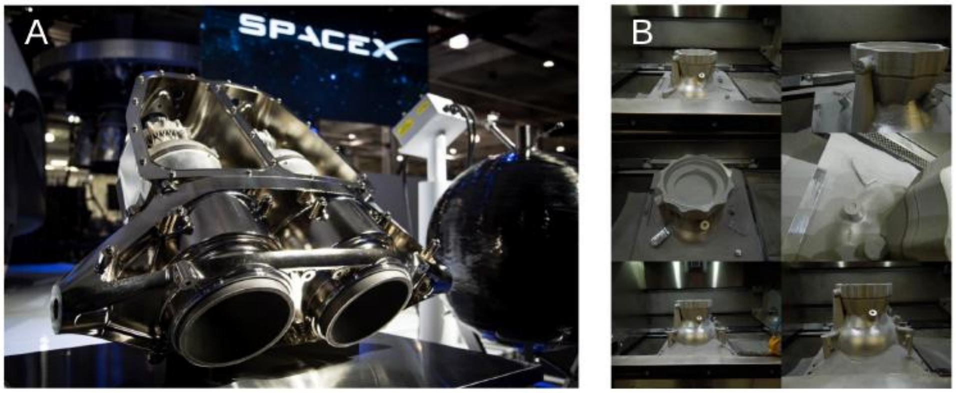

**Figure 2.4:** (A) completed SuperDraco engine [4]. (B) SuperDraco engine before removal from the EOS SLM machine [5]

Given all the various applications at NASA and SpaceX, there are certain common themes. The ability to produce mid-size high-temperature components for rocket engines is in high demand and additive processes are increasingly popular in research and commercial rockets. The current technology is limited primarily by build volume constraints. There are three species of materials under serious consideration for AM of rocket components:

1. Inconel. Used for its high strength at elevated temperatures and excellent oxidation resistance. This makes it ideal for contact with combustion gases or oxidizers. Commonly printed types are IN625 and IN718. [20]
2. Titanium Alloys. Exceptional strength with a density half of that of Inconel, Ti6-Al-4V is commonly used for structural elements in moderate temperature regions.
3. Copper Alloys. With exceptional thermal conductivity, copper alloys are used as a thermal material for liners and coolant channels. GRCop-84 was selected as a low-cost alternative to superalloys.[17][3]

# 3. Topology Optimization for SLM

## 3.1 Topology Optimization Methods

First introduced by Bendsøe and Kikuchi in 1988, topology optimization (TO) is the process of placing material in a discretized problem domain to optimally solve a design problem. This applies mostly to structural problems, however it can also be applied to other fields.

In general, this is a discrete optimization problem, as there is either material in a given cell (1) or not (0). Given this material distribution, a loss term $L_s$ can be calculated based on how well the current solution meets strength or compliance requirements. We can also add terms to the loss that penalize accessory properties like weight or volume. One can then come up with a total expression of loss that can be optimized using one of any number of techniques, as in equation 3.1.

$$L_{total} = L_s + \sum_{acc} L_{acc} \tag{3.1}$$

This discrete problem can be cast to a continuous problem via density methods, the simplest of which is the SIMP (Solid Isotropic Material with Penalization) [21]. In this approach, each cell is assigned a density between 0 and 1, and material properties are scaled by the density. A loss term is added that punishes the optimization for choosing intermediate values such that the final solution is close to binary. This allows the use of continuous optimizers which are generally better than discrete optimizers. The RAMP method is a more modern version of SIMP that improves on some optimization properties [22]. There are many more modern density-based algorithms. The discrete problem can also be solved directly using evolutionary algorithms, commonly known as Evolutionary Structural Optimization (ESO) [23].

## 3.2 Printing Constraints

The methods discussed in section 3.1 cannot be directly applied to additive manufacturing, as they would lead to structures that are either impossible to print or result in excessive print defects. Optimization of designs for SLM must take into account the restrictions of the process itself.

### 3.2.1 Minimum Length Scale

All additive manufacturing techniques have a minimum feature size. Feature size may be limited by several aspects of the printer, such as beam or feedstock diameter, or the precision of a motion axis. This must be taken into account during a topological optimization to ensure parts can be fabricated as designed.

There are several ways such a minimum feature size can be enforced. Many are based around the erosion and dilation filters from image processing, which when used in sequence can guarantee that any negative features smaller than the minimum feature size will be closed and small positive features will be removed [24]. The effect of these filters on a topology can be used to drive the optimizer towards a solution that satisfies the minimum feature size constraint [25].

### 3.2.2 Overhang Angle

Overhang angle is of significant concern in SLM. Large overhang angles can be responsible for several different kinds of defects.

Unmelted powder is a better insulator than the solidified material. As a result of this, melt pools created by a laser irradiating unsupported zones are generally larger than those created over supported regions. This can lead to the melt pool sinking into the powder, forming dross and lowering dimensional accuracy [6]. This is demonstrated in figure 3.1 A. Additionally, large melt pools can lead to droplet formation and lack of fusion [7]. These larger melt pools are demonstrated in figure 3.1 B.

Overhangs are also generally weaker than multiple layers melted together, as their cross-sectional moments of inertia, which scale with the cube of layer thickness, are much lower. This can lead to warping of overhanging structures, which leads to a lower quality surface finish and lower dimensional accuracy [6]. This is demonstrated in figure 3.1 C.

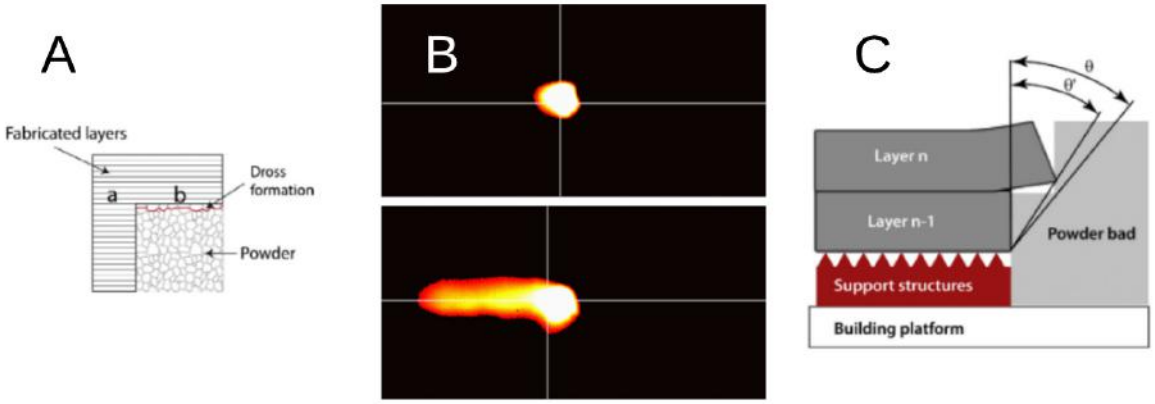

**Figure 3.1:** (A) Sketch showing how dross forms under overhangs. (B) Image of melt pools while lasing over previous layers (top) and an overhang (bottom). (C) Warping due to overhang. Figure adapted from [6, 7]

There are several ways overhangs may be accounted for in topology optimization. Langelaar proposes an algorithm that sweeps from the bottom to the top of the part, removing material that violates the maximum overhang. The amount of material removed can be used to punish the optimization, driving it away from the solution with illegal overhangs [26].

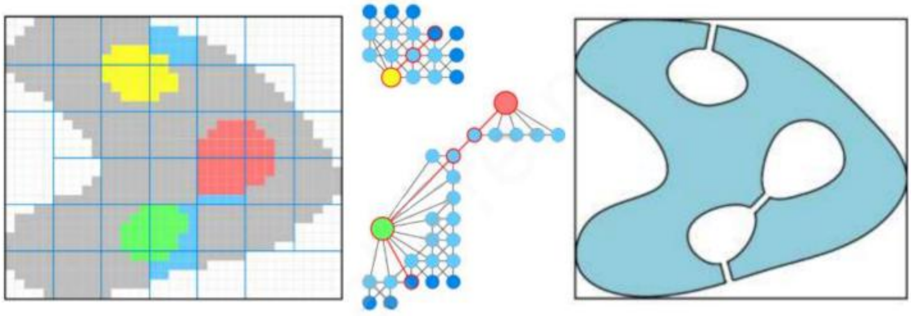

**Figure 3.2:** Void tunnel method using hierarchical graph pathing (reproduced from[8])

### 3.2.3 Voids

One downside of powderbed-based additive manufacturing processes is that the powder has to be removed from the part after printing is complete. This means topology optimization strategies must avoid producing enclosed voids in a part. This retained powder is especially troublesome for topology optimized designs since commonly the objective is to reduce the weight as far as possible and any powder not removed will increase the weight of the part and provide no additional structure [8]. Topologies consisting of enclosed voids are referred to as "multiply connected" in the literature and several strategies have been proposed to address the challenge of reducing these to simply connected equivalents.

A popular method proposed by Liu et al. is the virtual temperature method (VTM) [27]. This method formulates the void connectivity problem as one of steady-state heat conduction where a virtual heat source is placed at the center of each region of a multiply-connected structure. Low density ($\rho_e$=0) regions of the optimized structure are then given a high thermal conductivity whereas the remaining material is set to be insulating. Connectivity of voids to the outer boundaries will allow for heat transfer out of the part which minimizes this virtual temperature. Thus the void removal criterion can be expressed simply as a maximum temperature threshold, $T < T_{max}$ [27]. However, since this method requires solving an adjoint 2D heat conduction problem for each iteration it is very computationally expensive in practice [8]. Therefore, other methods have been developed. One popular method specific to ESO optimization is an approach of structural connectivity proposed by Xiong et al. [8]. This method categorizes each voxel by comparing the design variable to that of its neighbours to identify face-connected regions. To determine whether or not a particular region is a void or simply a cavity the algorithm evaluates the connectivity to the structural boundary. To do this efficiently, a hierarchical graph of voids is constructed and then used to pathfind locations of tunnels which connect the voids to the boundaries. A sample application of this method to a multiply-connected topology is shown in figure 3.2.

## 3.3 Lattice topology optimization

Imposing the manufacturing constraints on conventional TO algorithms can be both computationally expensive and lead to sub-optimal solutions [28].

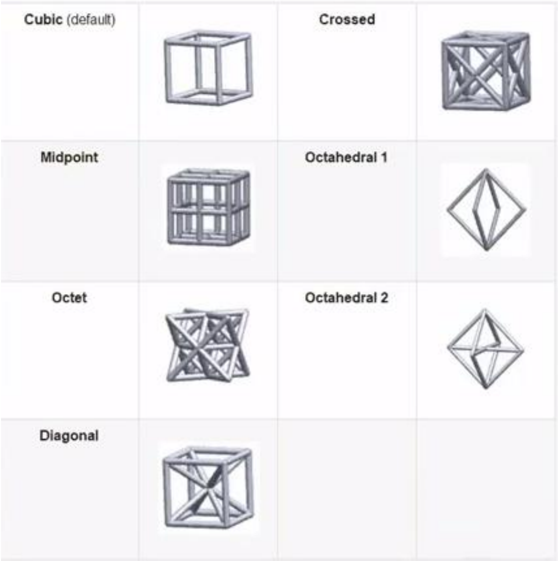

**Figure 3.3:** Lattice Types. From[9]

A solution proposed by Cheng et al. is using a self-supporting lattice cell as the basis of the optimized topology to directly address the AM contraints. In their paper, they suggest that conventional optimization algorithms such as SIMP, ESO, and level-set methods often result in significant overhang structures which require print supports that are difficult if not impossible to remove. Furthermore they argue that since standard methods solves the discrete 0/1 design problem by conversion of a continuous design variable (often relative density). The design space may contain a large number of intermediate values which are converted in in an ad-hoc manner.[28] The solution proposed by lattice methods is to maintain the shape of the optimization and instead alter the density continuously by defining a cellular infill structure which can be patterned throughout the component. The lattices used are generally open-cell and self-supporting which simplifies powder removal and eliminates overhang issues. This allows for computationally efficient TO since fine structures can be created without additional mesh refinement [29].

An example of the lattice types available in commercial TO solvers are shown in figure 3.3. For the TO solution to be efficient each lattice element is modelled not by individual strut geometry but instead as a holistic stress/strain response. The anisotropic response of each lattice type is determined through simulation and are of the form of equation 3.2.

$$\vec{\sigma} = C\vec{\epsilon} \tag{3.2}$$

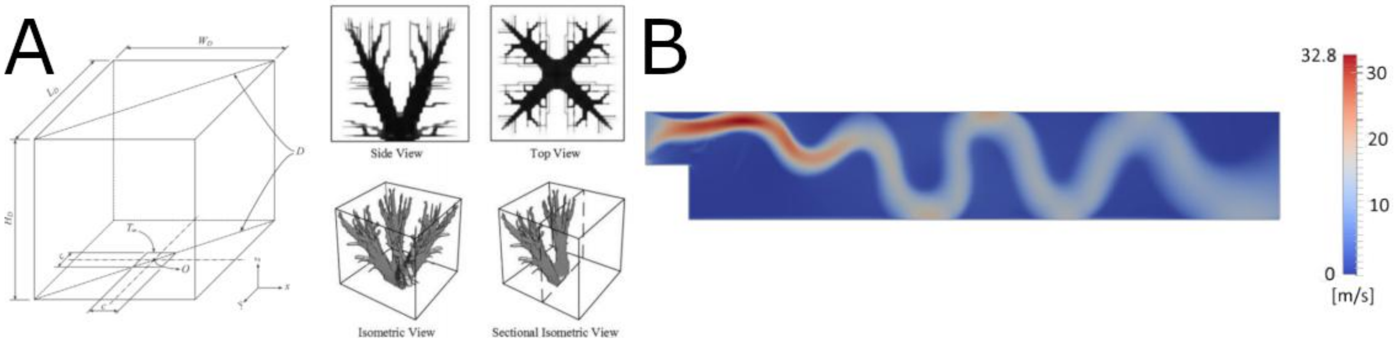

**Figure 3.4:** Optimal Heat Transfer Structures. A) 3D steady-state conduction solution from [10], B) Coupled heat transfer-CFD solution for optimal cooling channel from [11]

Where C is the symmetric 6x6 stiffness matrix with indices given as a function of the relative density of the cell [28].

$$C(\rho_r)_{kl} = a_1\rho_r + a_2{\rho_r}^2 + \cdots \tag{3.3}$$

To optimize the density of lattice structures, the solution is initialized at a uniformly high density. The relative density ($\rho_r$) of cells is modified at each iteration by changing the thickness of the cell struts. The solutions produced by lattice methods can occasionally result in excessively small features, so a minimum density constraint is often applied. This overall process of using macroscopic cell properties instead of direct modelling of the lattice structures is commonly referred to as the homogenization-based topology optimization (HMTO) and is common in commercial solvers [28].

## 3.4 Heat Conduction

A very recent area of interest for topology optimization is the maximization of heat conduction. These methods can be used in rockets for the design of efficient heat exchanger or fuel channel geometries. Common algorithms for topology optimization of heat transfer problems employ a gradient-based method such as the MMA (Method of Moving Asymptotes) optimizer[10]. Material density variation is generally achieved using a standard algorithm such as SIMP or ESO as discussed above. These solvers have been investigated for applications to steady state conduction problems as well as in CFD [10]. An example of heat transfer-optimized structure is shown in figure 3.4A where the a fractal structure can be seen.

A specific rocketry application for these methods is in the design of regenerative cooling systems. As previously mentioned, this method passes cold propellant through channels within the part to remove heat from the combustion boundary surfaces. The heat transfer rate to the coolant is given by equation 3.4, developed by Boysan et al. [30].

$$h_c = \frac{85.37C\rho\mu^{0.2}}{Pr^{\frac{2}{3}}}\left(\frac{G^{0.8}T_c}{d^{0.2}T_w}\right) \tag{3.4}$$

Given that the heat transfer varies at different points of the nozzle, the optimal solution is to dynamically vary the aspect ratio of each channel. While conventionally too difficult, additive processes can change aspect ratio as a function of thermal load along the nozzle to optimize between pressure drop and heat transfer yielding significant performance improvements[30]. Functional cooling channels made via SLM have been demonstrated down to 0.7mm [17]. These have the added benefit of rough internal surface texture which will cause flow in channels to be turbulent resulting in improved heat transfer.

Papers that investigate coupled heat transfer/flow optimization of coolant channels are relatively new. This is likely due to the computational complexity of such systems being extraordinarily high [11], on the order of 2x the computational time of a standard CFD simulation for each iteration. Pietropaoli et al. were able to successfully optimize small channel segments for heat transfer and pressure drop resulting in serpentine channels (figure 3.4B)[31].

# 4. Nozzle Design

To investigate the practical application of topology optimization, we consider a case study in the design of a new nozzle for Waterloo Rocketry.

## 4.1 Design Background

The SotS rocket is powered by a hybrid rocket motor with 38,000Ns of total impulse and a peak thrust of 5780N. The propellants are liquid Nitrous Oxide (NOS) as the oxidizer and solid Hydroxyl-Terminated Poly Butadiene (HTPB) as the fuel with aproximately 5% by weight aluminium powder additive. The nominal oxidizer-fuel ratio is 4.6 and the theoretical flame temperature of the combustion gasses has been computed using Rocket Propulsion Analysis (RPA) software to be 2960K. The engine is started using an electrical current passed through nichrome wire to ignite a puck composed of potassium nitrate (KNO3) and epoxy resin. This provides the initial activation energy to begin combustion since the propellants are not hypergolic.

### 4.1.1 Current Nozzle

The current SotS nozzle is a convergent-divergent nozzle with a 15°linear expansion section, a throat diameter of 40mm and an area expansion ratio (Ae/At) of 3.73. It is designed to maintain a chamber pressure of 400psi. The nozzle including the required liner and aluminium heat sink weigh a total 3.7kg. An overview of the full system is shown in figure 4.1.

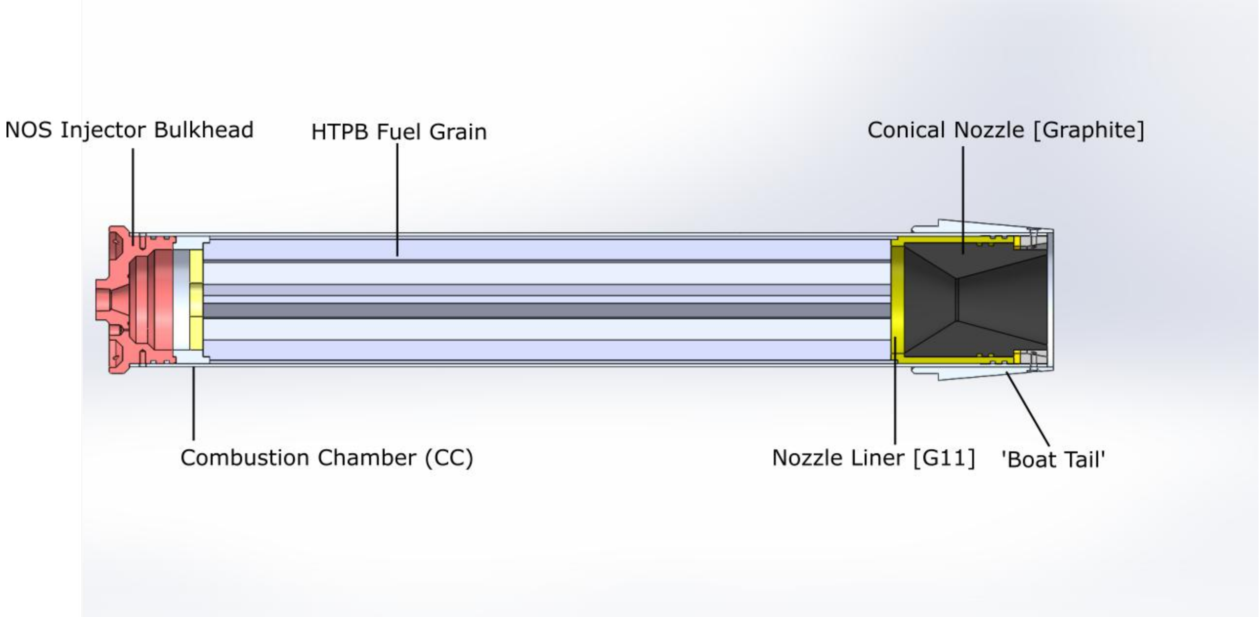

**Figure 4.1:** SOTS Nozzle

### 4.1.2 Problem Definition

The current design has the following limitations:

1. The material of the nozzle is graphite. While being relatively low density, machineable, and able to withstand extreme temperatures, it is a challenge for manufacturing. Machining graphite requires respirators and dust extraction since it produces very fine dust which is a potential safety hazard to both inhalation and slipping since graphite is a dry lubricant. In addition, the construction is sufficiently fragile that thin walls cannot be machined and as such the entire nozzle is machined out of a relatively heavy solid chunk.

2. The current nozzle flow geometry is far from ideal since it is machined by hand on a manual lathe. A linear expansion section loses up to 5% of the total engine performance compared to the common thrust optimized parabolic (TOP) nozzle geometry[13]. A more optimal geometry would be impossible to machine except on a multi-axis CNC lathe which the team does not have access to at this time.

3. Reusability. Due to the relatively soft yet brittle nature of the nozzle it can currently survive a maximum of 2 flights before needing to be remanufactured. Post-flight inspection has revealed chips taken out of the throat area and cracks in the sealing grooves. There is also a high risk of landing loads shattering the nozzle and as such the entire nozzle must be encased by the body of the rocket.

4. Thermal management. The heat load on the nozzle is very high, with the maximum thermal load at the throat of the nozzle exceeding $\frac{8MW}{m^2}$. While the current nozzle can handle these temperatures without issue, the aluminium

of the combustion chamber is at risk of becoming annealed at temperatures above 250C. The current solution involves a G11 fiberglass liner surrounding the nozzle to partially insulate it from the CC wall and a large aluminium “boat tail” that serves as a dual-purpose thermal mass heat sink and as an aerodynamic structure. This solution manages to keep the temperature of the chamber wall to below 120C but is very heavy [32].

## 4.2 Engineering Requirements

Based on these design challenges and the conditions experienced in the rocket testing and flight campaigns, criteria and constraints for the new design are created as follows in tables 4.1 and 4.2.

**Table 4.1:** Engineering Requirements

| Requirement | Operator | Value |
|---|---|---|
| Maximum design temperature | < | 1000C |
| Safety Factor | > | 1.8 |
| Thrust Load Supported | > | 4000N |
| Landing Load Supported | > | 4500N |
| System Weight | < | 3kg |
| Temperature Range | $\epsilon$ | (1-35)C |

**Table 4.2:** Constraints

| Constraint | Operator | Value |
|---|---|---|
| Max Linear Dimension | < | 250mm |
| Firing Inclination | < | 35° |

Criteria for the nozzle design were developed to codify the goals of the project based on the problems described in section 4.1.2.

- Minimize Weight
- Maximize Reusability
- Maximize Thermal Margins
- Maximize Ease of Assembly
- Maximize interchangability with current nozzle

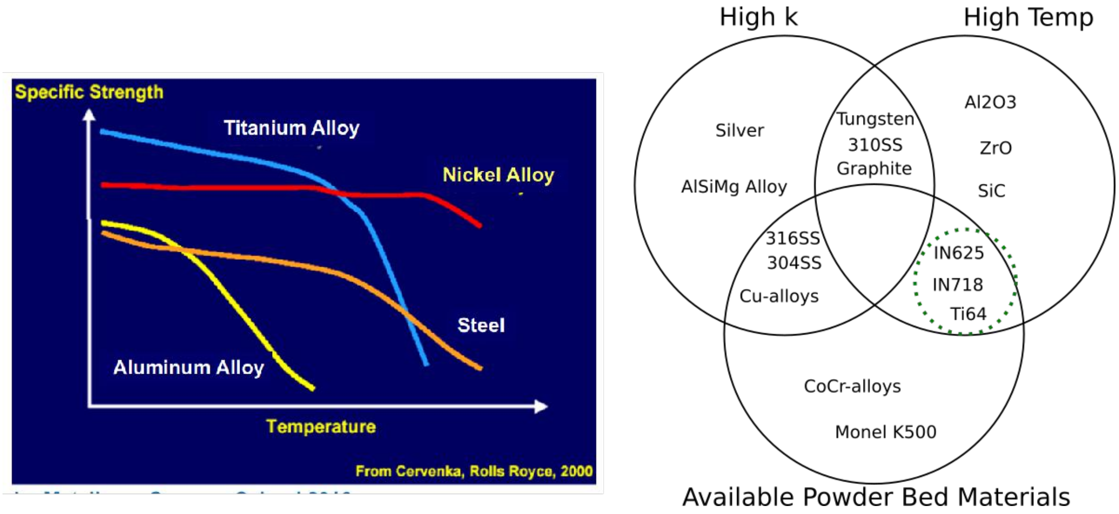

**Figure 4.2:** Material Selection

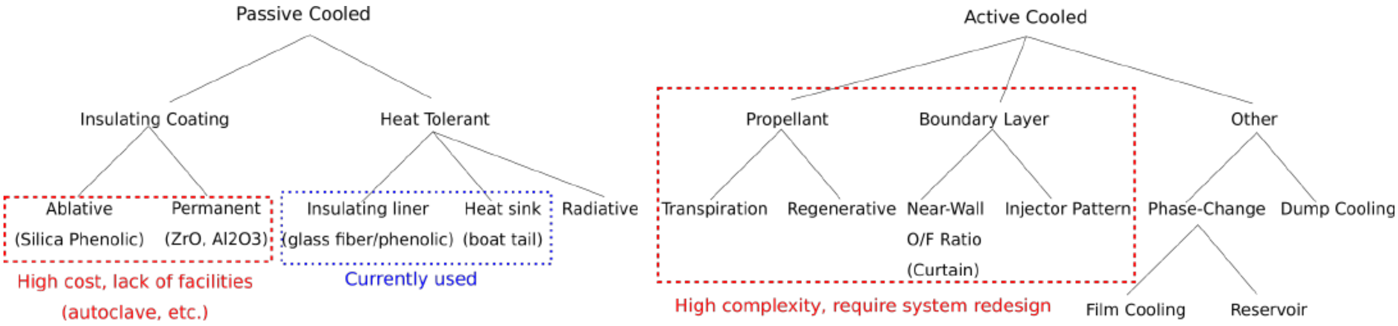

**Figure 4.3:** Morphological Chart

## 4.3 Design Selection

The possible design morphologies for cooling of rocket nozzles is summarized in figure 4.3. Using this chart we can see that without incurring a major redesign of the entire combustion section we are limited to non-propellant cooling methods which exclude traditional regenerative cooling systems. The further limitations in selection of morphology are the lack of composite/ceramic processing facilities, and limits due to the maximum operating temperature of materials available for SLM. These limitations exclude insulating coatings and heat tolerant designs respectively. The primary options are liquid phase-change or dump cooling where a non-propellant fluid is used to absorb heat from the nozzle walls and is either dumped or boils off during flight. Due to the short burn time of the Kismet engine a dump cooling system and a phase-change method will perform very similarly. Applying the design criteria of minimal weight and maximized ease of assembly it is beneficial to avoid the plumbing and external reservoir required by a

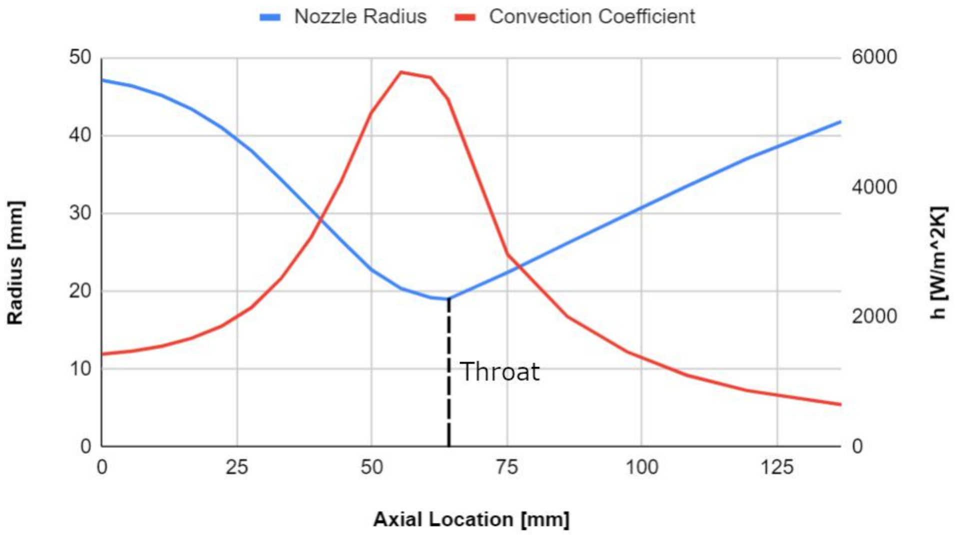

**Figure 4.4:** Convective Coefficients Within the Nozzle

dump cooling system.

Therefore, a liquid phase-change cooling solution will be pursued in this design. The material selected for the nozzle is Inconel 625 due to its exceptional oxidation resistance, common use in literature, and strength at extreme temperatures as shown in figure 4.2.

### 4.3.1 Cooling Method

At full thrust, the rocket nozzle encounters a thermal load in excess of 80KW as computed using RPA. The total burn time of the engine is 12.5 seconds [32] giving a total thermal energy on the order of 1MJ. Convection coefficients for supersonic flow through the nozzle were computed using the semi-empirical correlation given by Bartz [13]:

$$h_g = \frac{0.026}{D^{0.2}}\left(\frac{c_p\mu^{0.2)}}{Pr^{0.6}}\right)(\rho v)^{0.8}\left(\frac{\rho_{am}}{\rho'}\right)\left(\frac{\mu_{am}}{\mu_0}\right)^{0.2} \tag{4.1}$$

As can be seen in equation 4.1 the heat transfer rate is a function of the nozzle diameter and flow velocity, both of which are non-linear functions of the position along the nozzle. RPA was used again to evaluate the correlation at many points along the nozzle axis as shown in figure 4.4. The heat transfer rate is maximum at the nozzle throat and steeply tapers off as the flow expands. The suitability of cooling morphologies determined in section 4.3 limited the design to either dump or phase-change cooling. Within these categories there are several approaches. For dump cooling the most common by far is to create small high-aspect ratio coolant channels throughout the nozzle for the coolant to be pumped through. This option was removed by the criteria of maximizing interchangeability with the current rocket design since it would have required an on-board coolant reservoir and pumping system. The remaining options are therefor as shown in figure 4.5. Given the criteria of maximizing heat transfer while minimizing weight the self-supporting lattice (B) was selected. It is assumed that this solution will allow for a maximum contact area for heat transfer to the coolant while allowing for use of minimal hot wall thickness. To validate this assumption, it will be compared to a traditional topology optimization solution run for type A to evaluate which gives a lower weight and higher heat transfer.

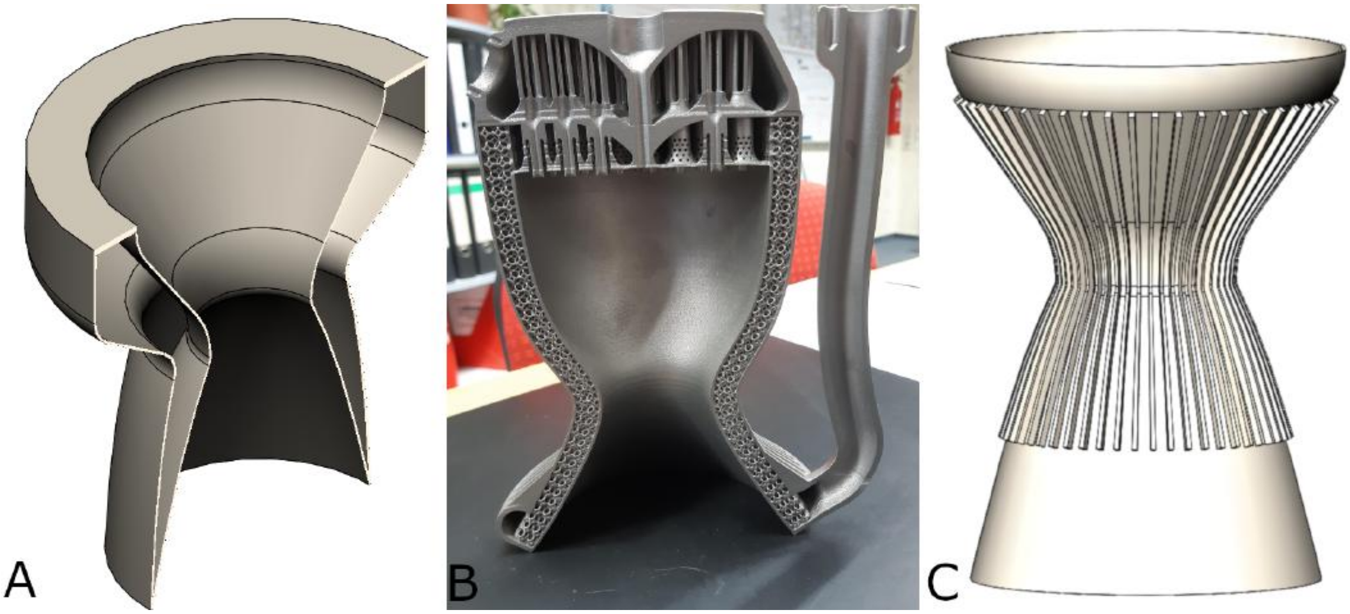

**Figure 4.5:** Phase-Change Cooling Options. (A) Plain shell geometry, (B) Self-supporting lattice [12], (C) Cooling fins

## 4.4 Supersonic Nozzle Geometry

The internal geometry of the nozzle uses the Thrust-Optimized Parabolic (TOP) geometry defined by Rao [33]. This geometry is a parabolic approximation to the ideal contour designed via the method of characteristics which computes optimal flow expansion by considering the turning of shockwaves within the nozzle. The TOP geometry strikes a balance between efficiency and overall nozzle length (and by therefore weight) and is widely used in modern rocketry[13]. The parameters of this nozzle are shown in figure 4.6 and were optimized using Rocket Propulsion Analysis software (RPA) to meet the inlet pressure and critical massflowrate properties of the Kismet hybrid engine developed by Waterloo Rocketry [32]. The results of this optimization are shown in appendix A figure A.1. The divergence efficiency of this nozzle approaches 99% while being 15% shorter than the previous nozzle generation.

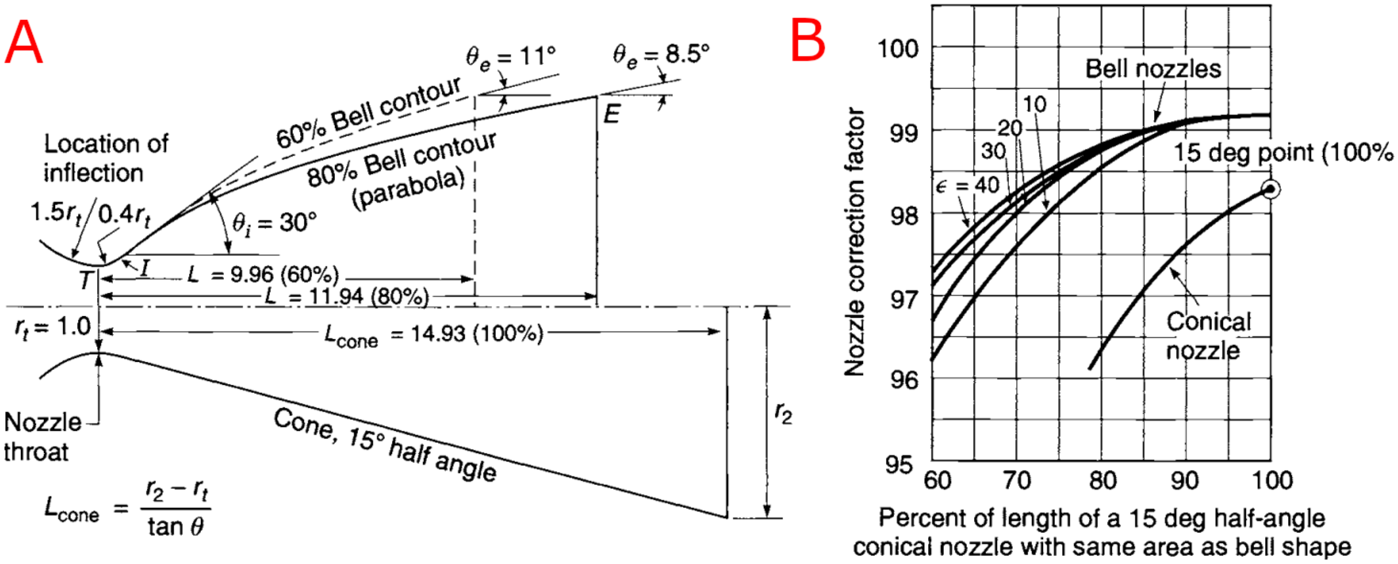

**Figure 4.6:** A: Comparison of Nozzle Types [13] B: Nozzle Efficiency Coefficient vs. Length reproduced from [13]

## 4.5 Topology Optimization

While the functional geometry of the nozzle is essentially fixed, the structure of the nozzle is a non-trivial trivial design problem since it must be extremely lightweight while supporting both pressure and thermal loads. This is an ideal place for the application of topology optimization. ANSYS 2020 R1 was selected as the platform for performing topology optimization due to its integrated additive manufacturing constraints. Transient thermal loading cannot be fed into the optimization and as such the structure will be optimized for static mechanical loading. Another constraint on the optimization process was the available computational resources which required careful simplifications to reduce computational costs. A high-level overview of the process flow used is shown in figure 4.7. To perform this optimization, a CAD model was created with the minimal allowable hot wall thicknesses and a fully filled internal structure. This internal chunk of material defines the optimization region where material can be removed by the selected TO algorithm. The model loads were defined based on the expected 700psi maximal inlet pressure based on prior engine test data. The remaining pressure loads were scaled to the inlet pressure based on simulations done in RPA. The complete loading diagram and mesh for are shown in figure 4.8.

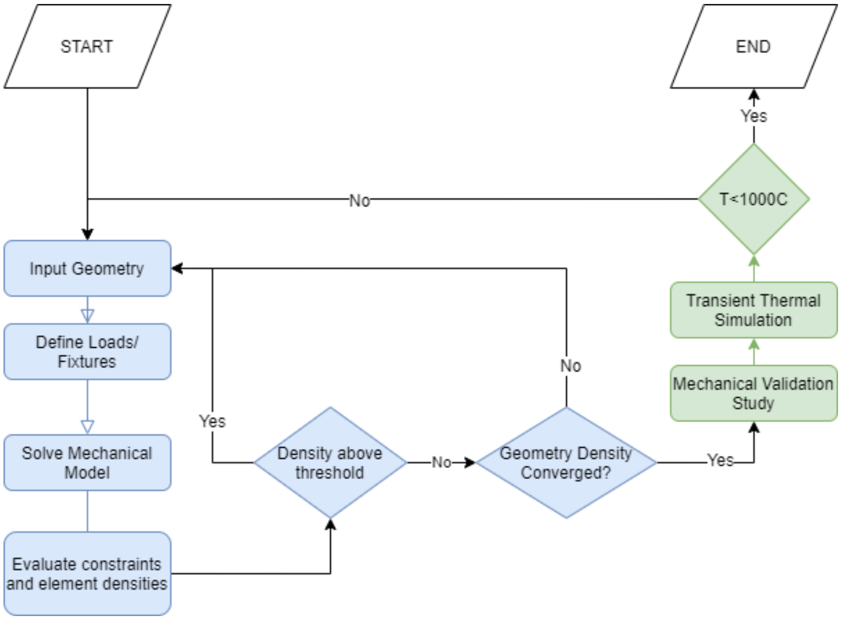

**Figure 4.7:** Optimization Process Flowchart

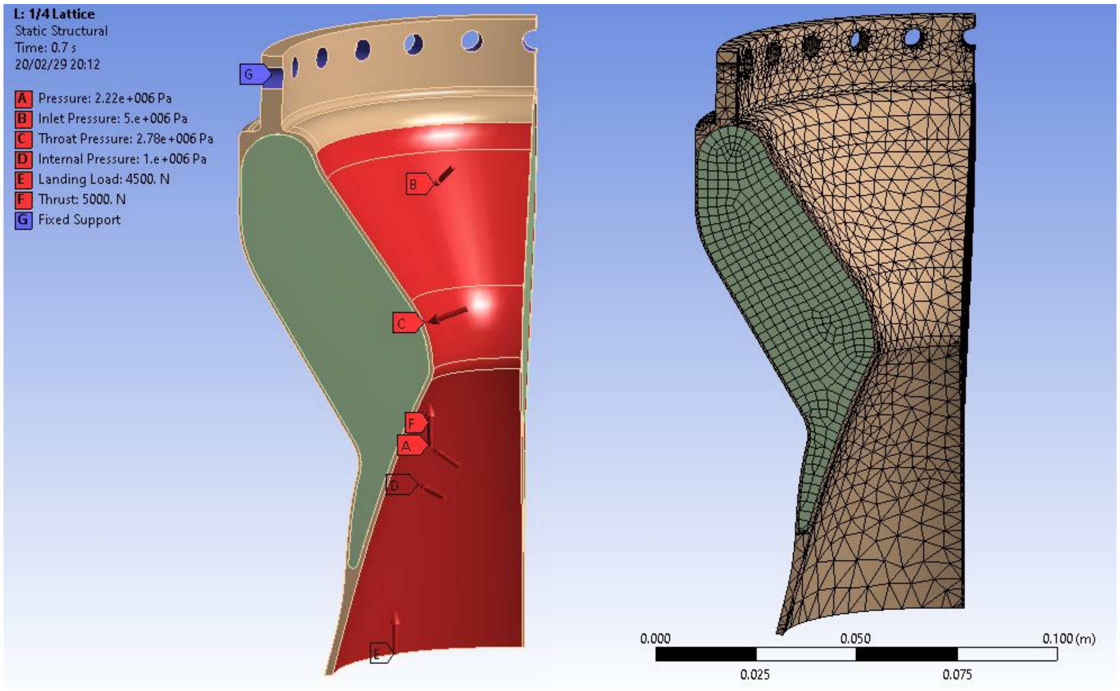

**Figure 4.8:** ANSYS Model

This model uses symmetric boundary conditions in both X and Y to reduce the number of elements to be simulated. Axial loads were added to model the thrust produced by the engine and the shock loads experienced by the nozzle when the rocket lands (as defined in the requirements).

### 4.5.1 SIMP

The first method investigated was a density-based method with additional additive manufacturing overhang and minimum feature size constraints as discussed in section 3.1. The overhang angle in the build direction and the minimum feature size were set to 45°and 2mm respectively. The stiffness penalization applied in the SIMP algorithm was set to a factor of 3. The simulation was run on 1/8 of the total geometry with a cyclic symmetry boundary condition to reduce the size of the computational domain. The simulation converged after 59 iterations to the result shown in figure 4.10 A. The resultant geometry makes contact with the surface at only a few points, leaving large areas completely without support. While this a sufficient solution to the stresses within the part this may pose some challenges in heat transfer due to lack of surface area in contact with the fluid and large wall thicknesses in others.

An consideration of note for SIMP optimization is that the results can be heavily dependant on the mesh size and initialization of the density due to the tendency of this algorithm to converge to local minima [34].

### 4.5.2 Lattice Optimization

The second approach used was a lattice-based optimization using an octahedral unit cell. This type was selected as it is the only lattice available (figure 3.3) which meets the 45°printer overhang constraint. The lattice optimization method implemented in ANSYS is based on the variable density HMTO approach presented in [28]. There are two further parameters which must be determined for the design prior to running the optimization. These are the lattice cell size and minimum lattice density. The minimum lattice density was selected as 0.13 based on a minimum desirable feature size of 700$\mu$m. This value was selected based on acceptable porosity defects on lattice elements printed at 45 degrees based on results presented in figure C.1 [14]. To select the lattice cell size, we can perform a rough approximation for the spacing of supports using the simply supported plate loading formula in equation 4.2 [35]. For a hot wall thickness of 1.3mm and a inlet pressure of 5MPa, this gives a maximal lattice size of 10.7mm. Given the desired safety factor of 1.8, this sets the upper limit for cell size at 7mm.

$$\sigma = \frac{0.75pa^2}{2.62t^2} \tag{4.2}$$

The simulation was run with a mass minimization objective using a global von-mises stress constraint until a convergence of 0.5% was reached, taking 20 iterations. The plot of optimized lattice density is shown in figure 4.9. This shows that the highest lattice density occurs near the throat which is intuitively reasonable since this is where pressure stresses are highest. Another interesting feature of the optimization result is a slight asymmetry at the very top. This is likely due to the spacing of the bolts used to support the nozzle.

Given that the selection of the lattice cell size was somewhat ad-hoc it is important to validate the selection of this parameter. A second lattice optimization was run for lattice cell sizes l=10mm to establish whether a larger lattice

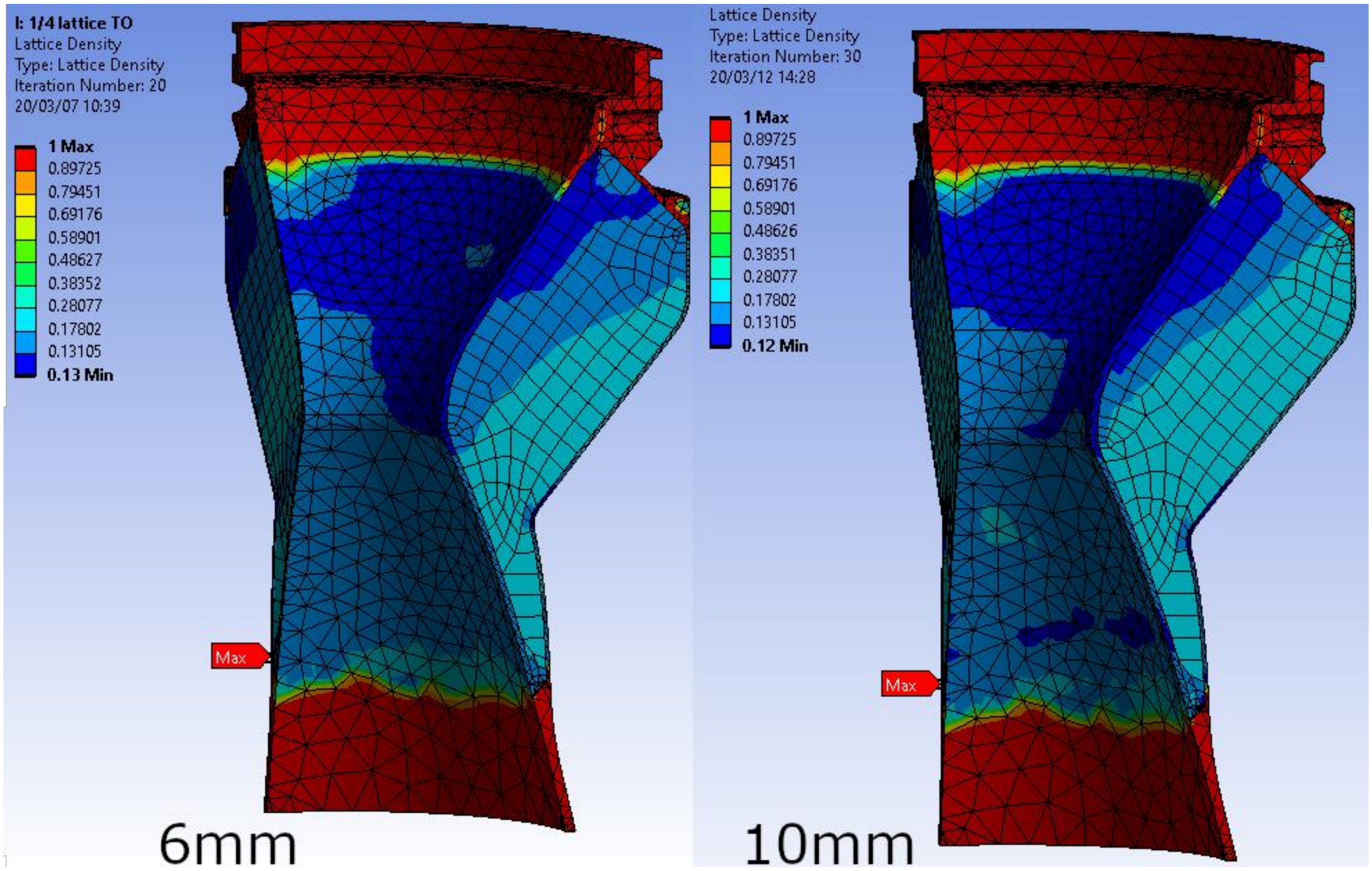

**Figure 4.9:** Lattice Density Plots for Varying Lattice Size

could still meet the stress constraints with an optimal weight. The larger lattice solution is approximately the same average density and overall the solutions look very similar. However the larger lattice has a slightly higher density in the near-throat region. This is reasonable since a larger lattice size will place more stress on individual members, requiring them to be larger.

The resultant lattice is shown in figure A.5 and the overall weight of this solution at 204grams is 11% more than that of the smaller lattice. This demonstrates that the specific strength of the smaller lattice is higher and thus yields a more optimal solution. An interesting note is that the larger lattice solution took an additional 10 iterations to reach convergence, suggesting there is greater instability in the solution process.

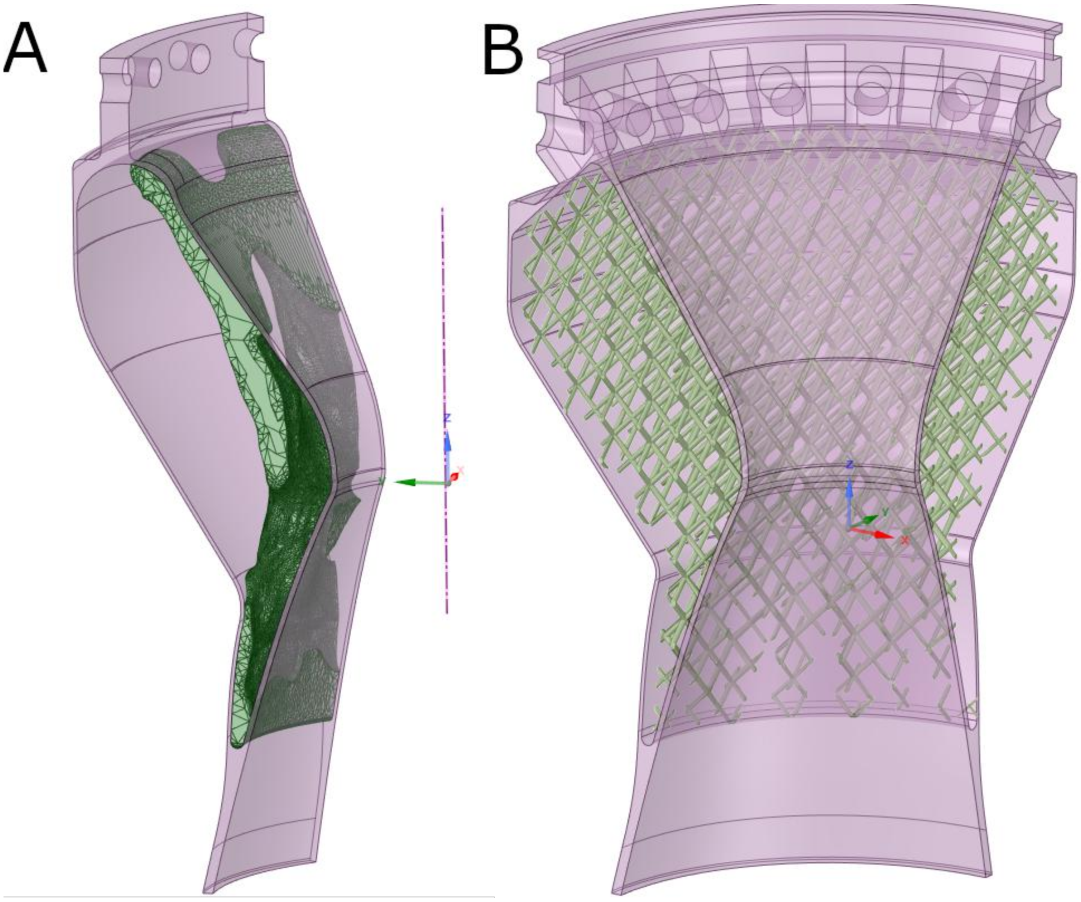

**Figure 4.10:** Optimization Results: (A) Density Based (B) Octahedral Lattice-Based

### 4.5.3 Optimization Results

Comparing the results in figures 4.10 we observe that they are both essentially axisymmetric. This is expected since the applied loads are all assumed to be symmetric. Furthermore, the lattice solution is overall significantly lighter, with the internal structure weighing in at a total of 184g compared with 800g for the density optimized approach. Another interesting difference between the simulations is the computational cost of both simulations. The SIMP algorithm required 59 iterations to converge with a total computation time of 14 core-hours whereas the 7mm lattice-based method required only 20 iterations and 1.5 core-hours. This is consistent with the results of [28] since SIMP requires a mesh on the order of the smallest feature size whereas lattice methods can use a much coarser mesh on the order of the lattice cell size. Convergence plots for both methods are shown in the appendix, figures A.2 and A.3.

The large discrepancy between the weight reached by these two solutions suggests that the problem is best solved using fine structures and that the SIMP solution did not have sufficent mesh resolution to produce a efficient solution.

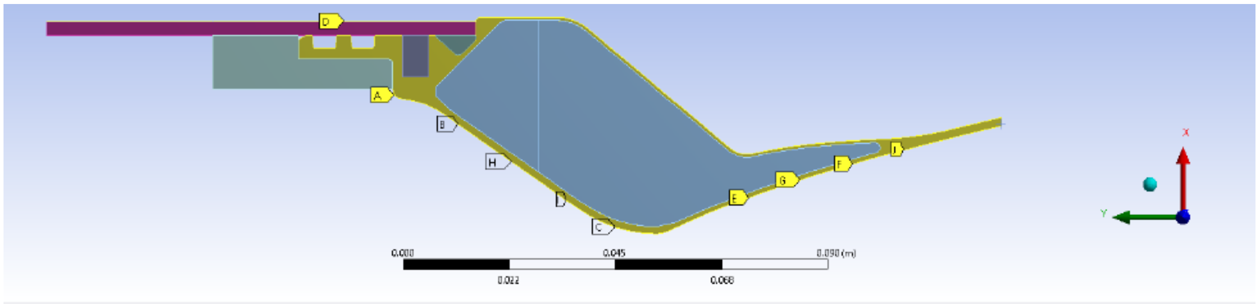

**Figure 4.11:** ANSYS 2D Thermal Validation

### 4.5.4 Thermal Validation

To verify which optimized result best achieves the goals of the design, a validation study was performed for both transient heat transfer and for mechanical strength.

The first important validation is to compute the thermal performance of both optimization results and determine if they are suitable. Convection coefficients determined from RPA in section 4.3.1 were applied to the model in a transient thermal study for the full burn duration of 12.5seconds. Due to computational size constraints, it was not possible to model the entire problem in 3D due to the non-linearity of the materials involved. As such, the simulation will be reduced to a 2D approximation with the reasoning that the internal lattice structure will only improve the heat transfer from the wall to the coolant. This reasoning is based on the fin efficiency equation 4.3[36].

$$\epsilon_{fin} = \frac{q_f}{hA_c\theta_b} \tag{4.3}$$

For $\epsilon > 1$ the heat transfer with fins exceeds the heat transfer of the plain surface. Using the thermal conductivity of inconel it can be computed that a 1mm diameter pin fin (an approximation of a lattice member) will have an efficiency of 1 at a minimum length of 0.5mm as shown in appendix figure C.3. Given that the lattice struts are on the order of the lattice size (7mm) we expect the fin efficiency to exceed 1 at all points of the nozzle. Therefore to save computational complexity we can assume the lattice solution performs on-par or better than a plain shell due to this effect. The model used to run thermal validation is shown in figure 4.11. It should be noted that due to the phase change occurring within the coolant a full validation is only possible via multiphase CFD of the 3D problem. However, this was not possible due to the aforementioned computational resource constraints.

Figure 4.12 shows the maximum temperatures reached by the lattice design at the end of the engine burn. The SIMP solution shown in figure A.4 performs notably worse here.

The maximum temperature reached by the lattice result is 1005C at t=12.3s which just barely meets the requirement. The SIMP result reaches upwards of 1060C at the same time point, notably at a different point slightly upstream of the throat. This is likely due to the thick wall sections at this point that are created by the SIMP result which prevents the efficient transfer of heat to the coolant. This is in part due to the low thermal conductivity of Inconel relative to other metals.

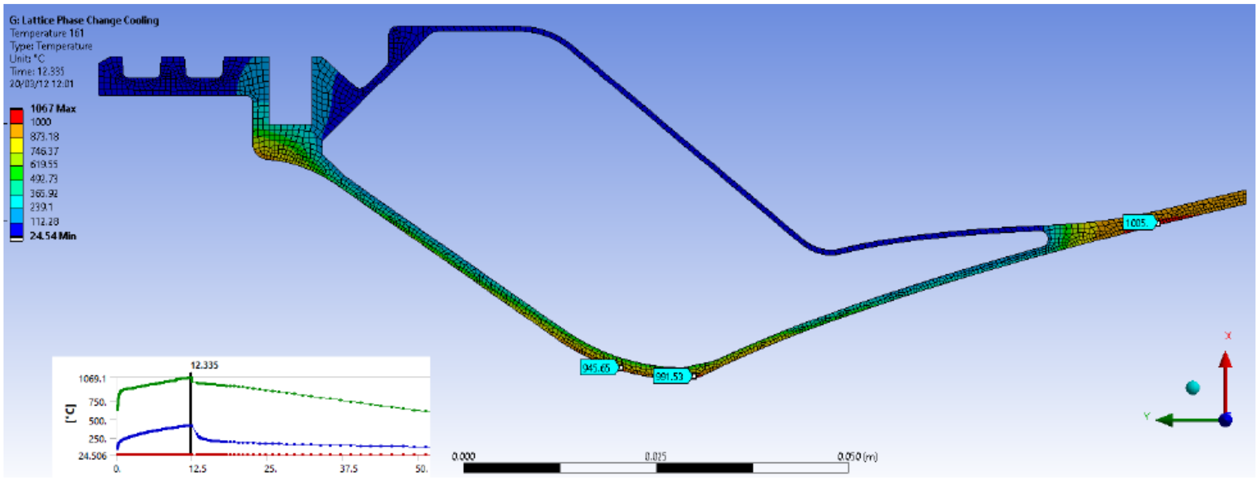

**Figure 4.12:** Lattice Thermal Performance

### 4.5.5 Mechanical Validation

For the mechanical validation, the allowable stresses are taken based on the mean properties as-SLM material from the Renishaw datasheet. An interesting consequence of SLM is significant anisotropy on the order of 20% lower along Z than in the XY plane [37]. This is a result of the grain structure formed during laser melting which forms columnar grains parallel to the build direction as a result of the thermal gradient in the z direction leading to epitaxial growth. [38]. The allowable von-mises stress was conservatively selected using on the average of the XY and Z strengths since the pressure loading is predominately in the XY plane. Using a safety factor of 1.8 we define the following allowable stress regions based on the expected temperature. The expected temperatures are conservative limits based on the thermal study performed above.

- For the throat area which reaches nearly 1000C, the allowable stress is 97MPa
- For the other hot-wall regions we will conservatively use the strength at 870C, giving an allowable strength of 195MPa.
- For all other regions with only indirect thermal loading (outer wall, lattice etc) we will assume a maximal temperature of 750C which gives an allowable of 290MPa.

A full plot of allowable stress versus temperature is provided in figure C.2. The results of the validation studies are shown in figure 4.13.

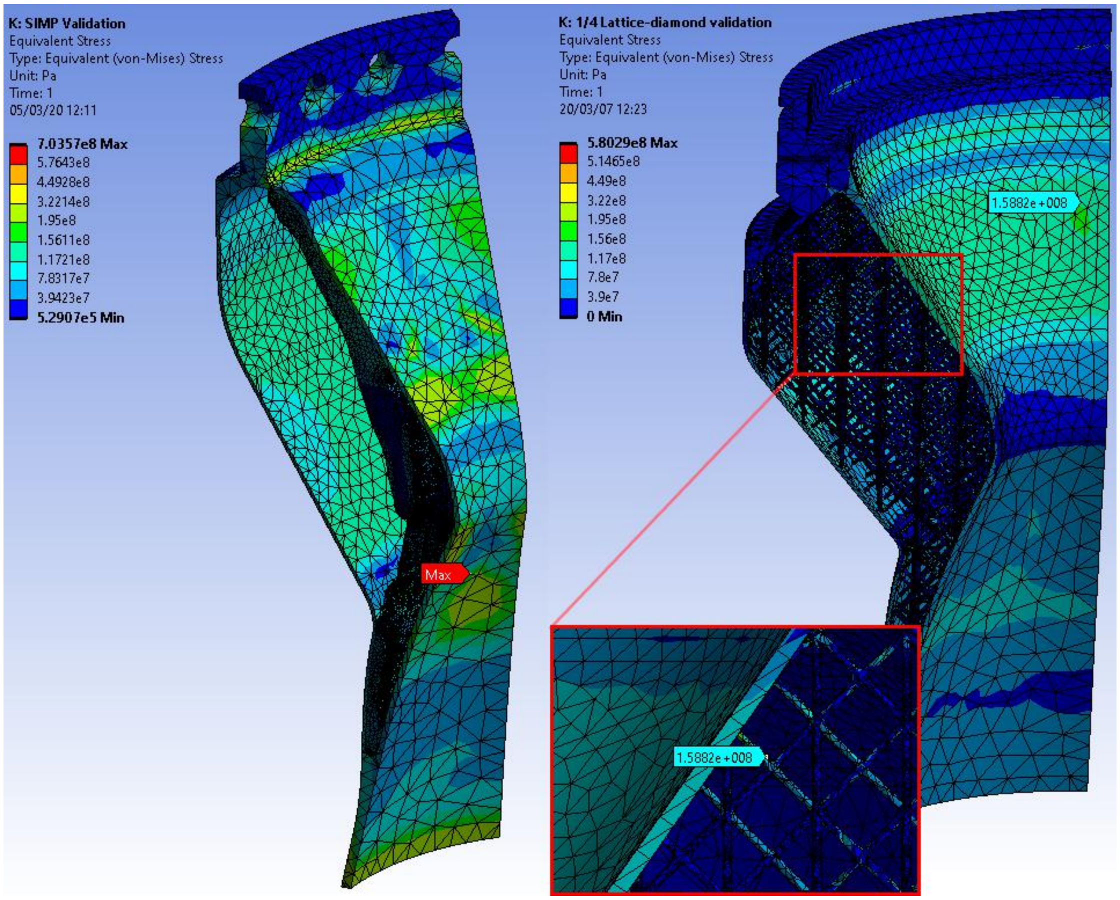

**Figure 4.13:** Validation Study (A) SIMP, (B) Lattice

Due to the complex geometry there are some mesh inconsistencies which have single elements reaching stresses of 500-700MPa. Given that these only occur at the contacts with the outer wall and are very localized to small elements it is likely that these are numerical issues in the solution and unlikely to represent actual yeilding. These will be investigated with a grid refinement study.

Rejecting these few outliers, the maximum stress for the lattice solution occurs on the contraction wall and is 158.9MPa, representing a safety factor of 2.2 against yielding based on the as-SLM material properties. This is slightly higher than the design safety factor which could suggest that the optimization was stopped at a local minima as opposed to the global minima. This is a common error in topology optimization algorithms which is quite difficult to remove [39]. Another possible reason for this could be the lack of resolution in the topology optimization model as compared to the validation system. Given the minimum lattice size constraint a smaller lattice would only increase the weight compared to this solution.

The SIMP solution is much closer to the 1.8 design safety factor but again shows some amount of outliers.

## 4.6 Validation of Requirements

The following list is a summary of the validation that the selected design meets the requirements defined in section 4.2. In addition to the requirements, mesh convergence was checked for the stress results.

1. Maximum temperature < 1000C: Met by thermal validation study, figure 4.11
2. Safety Factor > 1.8: Demonstrated 2.2SF against yielding in figure 4.13
3. Thrust Load Supported > 4000N this was included in the stress validation study above.
4. Landing Load Supported > 4500N. Since this load is not present at the same time as the thrust and the nozzle should have cooled down significantly by the time the rocket lands, this load was validated in a separate study and compared to the allowable stress at 200C, giving a minimum safety factor of 3 as shown in figure B.1.
5. System weight is 2200g, significantly less than the 3kg target.
6. Temperature range. A thermal simulation was run for $T_{amb}$=35°C with negligible increase in maximum temperature. To handle cold temperatures, antifreeze will be added to the nozzle coolant water which will make it suitable for use down to -20°C.
7. Firing inclination- at 30 degrees the estimated coolant level at the end of the burn will not leave the throat without coolant as shown in figure B.2. Plugs will be used in the lower vent holes to retain the coolant.
8. Max dimension of the nozzle is the height at 150mm. This is well within the build volume of the printer.
9. Mesh convergence. To validate that stress results were mesh-independent, a study was run with 2x mesh refinement which showed nearly identical results (figure B.3).

### 4.6.1 Design For printing

The print was intended to be run on MSAM's Renishaw AM400 SLM system using the machine default parameters for Inconel 625. The layer height will be 60 $\mu$ m. Throughout the design process, there were a few instances where DFM was required to adjust the geometry to the limits and process of the AM400 machine. Powder removal was considered during the design process and set a practical lower limit on lattice cell size. Excessively small lattice elements would be likely to entrap powder and require significant flushing to remove it which would be nearly impossible considering the enclosed geometry of the nozzle. Another important consideration was the top structure of the part which encloses the inner volume. Originally this had been designed to have a full radius, however due to the large unsupported area print quality may have suffered. As a result, it was changed to converge from both sides at 45 degrees meeting at a small 1.5mm flat. Another change required was the modification of a o-ring sealing groove. By selecting a thinner o-ring the overhang length could be greatly reduced while retaining adequate sealing. A summary of these design changes is presented in figure 4.14.

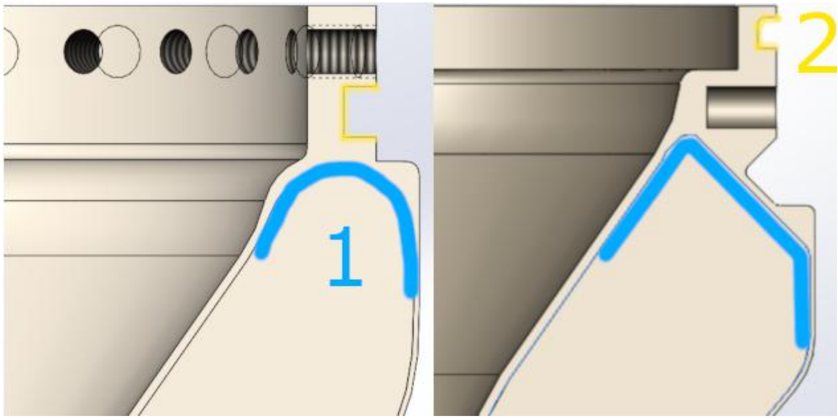

**Figure 4.14:** DFM Changes

## 4.7 Results

Figure 4.15 shows the results of the design including the integrated mounting and sealing features. Unscintered powder will be removed using compressed air, percussive impacts and flushing with water. Regrettably, unforseen circumstances prevented MSAM from completing this print since the lab was shutdown due to Covid-19. This nozzle is due to be hot fired once it is completed to perform a final validation of the thermals and the performance impacts before it flies for the first time. The internal and external surfaces of the nozzle will require some sanding to ensure they are smooth and do not disrupt the flow pattern either inside the nozzle or create additional drag while in flight.

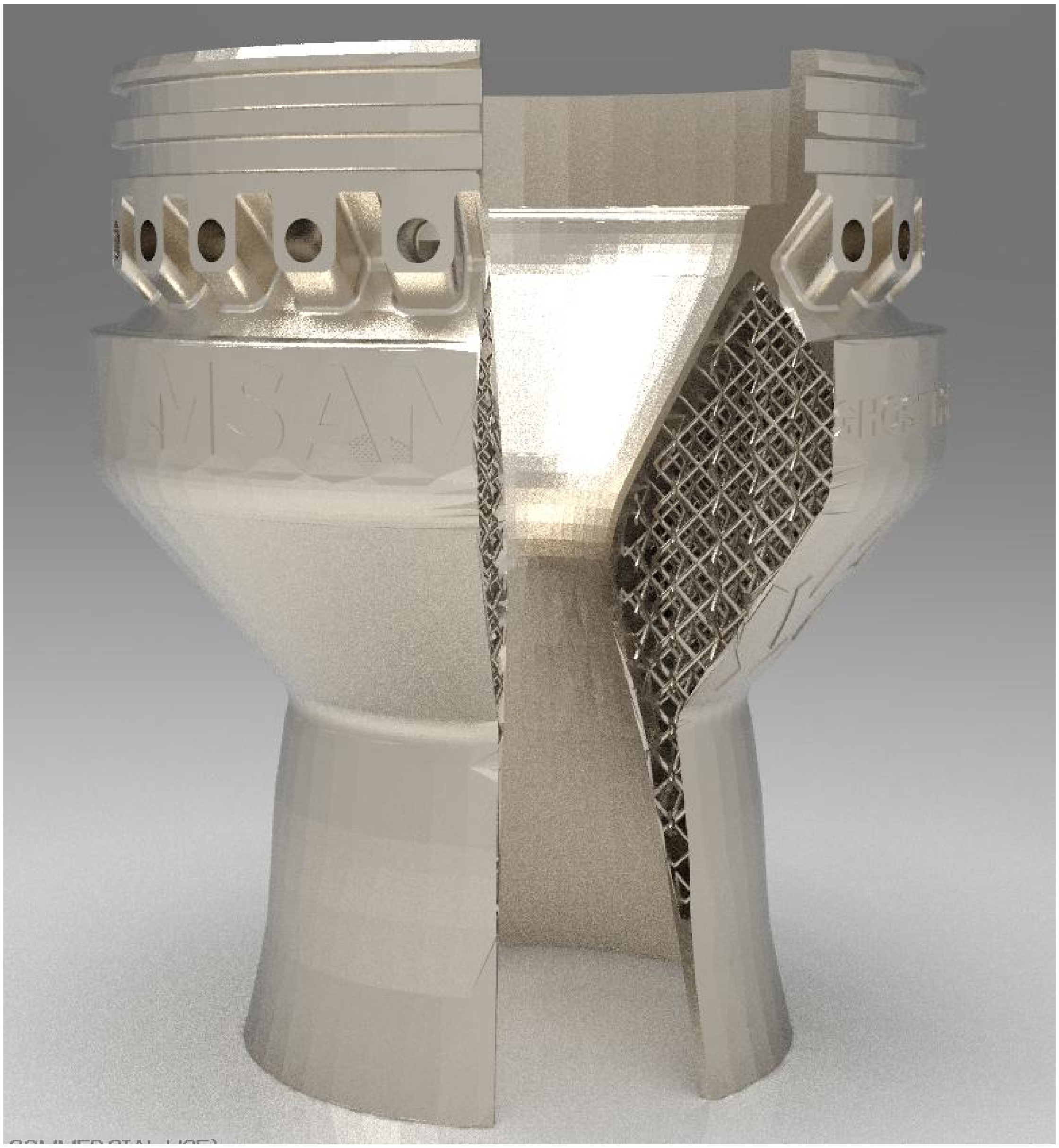

**Figure 4.15:** Sectioned Render of Design

### 4.7.1 Rocket Flight Impact

The total weight savings with the new design amount to 1515g, primarily attributed to the integration of the mounting features and removal of the large aluminium "boat tail" heatsink. It should be noted that the mass of the nozzle will decrease during flight due to boil off but this rate is difficult to predict. As simulated in RPA, the specific impulse of the engine will be increased by 3 seconds or 1.5% due to the new geometry. Combined these effects have a non-insignificant improvement on the altitude performance of the rocket. Figure 4.16 shows a comparison of the simulated apogee of the rocket with the new nozzle as compared to the old design. We can see that the apogee is increased by a total of 213m, or 2.5%. This may seem like a small gain, however in the world of rocketry a single percent improvement is a large achievement, especially where engine development is concerned.

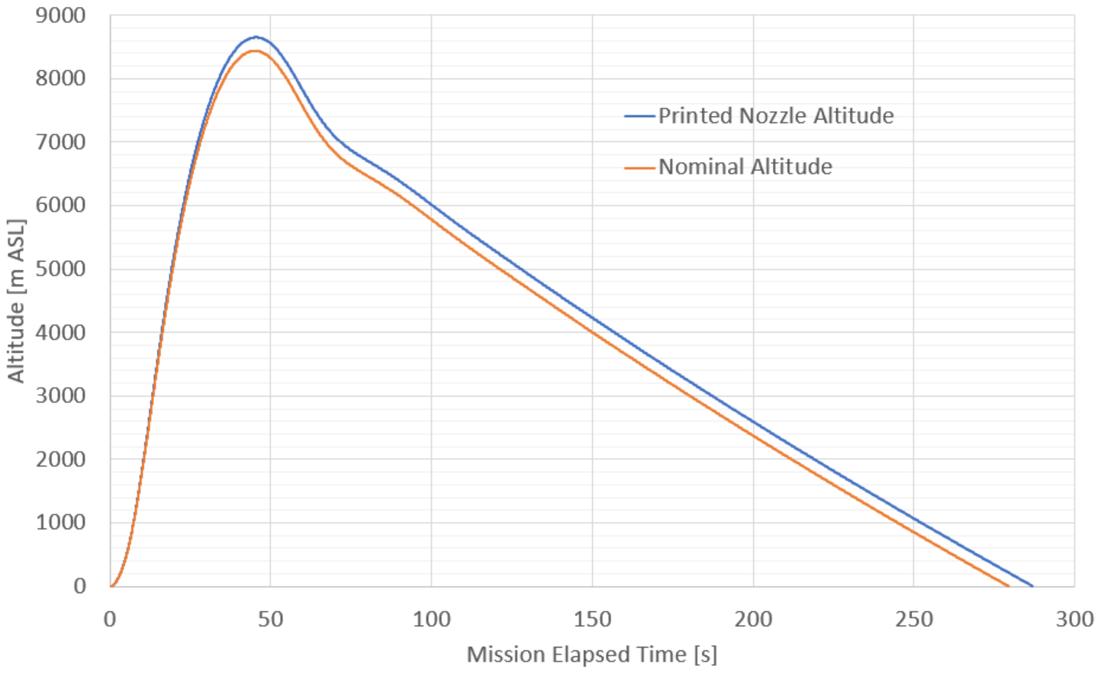

**Figure 4.16:** Altitude Improvement

### 4.7.2 Future Work

There are several limitations of this work which may be addressed by future efforts on this nozzle project.

- Due to limitations of computational complexity it was not possible to cover all aspects of the topology optimization for this structure. Work is needed in mesh refinement on the SIMP result to properly establish grid independence of the result and ensure that sufficiently fine features can be resolved. This work also did not consider the commercially available level-set TO methods. Future works should investigate the solutions produced by these methods as compared to the results of this paper.
- For validation, a full model thermal multiphase CFD of the nozzle would ideally be performed before any hot-fire testing takes place. This is expected to be incredibly costly computationally since it requires solution of

coupled 3D Navier-Stokes and general 3D heat equations with phase change mass transfer. It is unknown if k-$\epsilon$ turbulence modelling will produce a satisfactory result and therefore even more expensive methods such as LES may be required. Therefore, an alternate solution would be to run a sub-scale burn of a shorter duration and use high-temperature thermistors to compare the the thermal model against experimental results before moving to full duration firing.

- Finally, in this work, a BCC lattice was used. This was due to limited cell types available within ANSYS. However, research has shown that a FCC structure with additional vertical supports (FCCZ) can provide more than double the strength to weight ratio for a given lattice volume as shown in figure 4.17 [14]. Future projects should attempt to implement this structure since it will likely provide a significantly stronger result. The lattice solver in ANSYS does not support local definitions of stress constraints, and as a result the entire lattice was optimized using a global definition based on the minimum allowable stress. For a truly optimal result the strength criterion should be set based on the temperature of each section by sectioning the lattice result. However this may yield practical difficulties in generating the lattice geometry and the weight savings for such a small volume would likely be minimal.

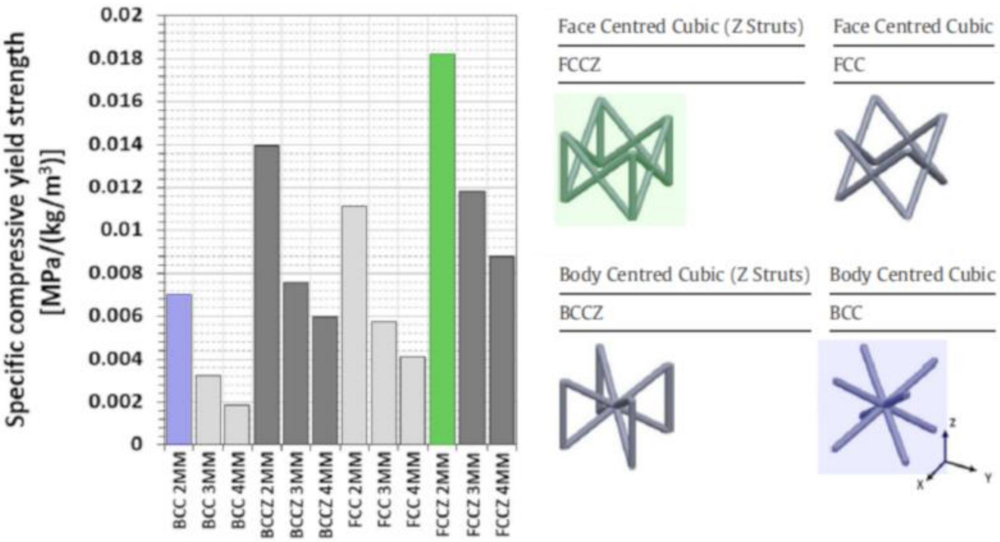

**Figure 4.17:** Lattice Specific Strength from [14].

# Bibliography

[1] NASA, "Space shuttle main engine enhancements," 2000.

[2] D. De Almeida and C. Pagliuco, "Development status of the l75: A brazilian liquid propellant rocket engine," *Journal of Aerospace Technology and Management*, vol. 2, pp. 475–, 12 2014.

[3] P. R. Gradl, S. E. Greene, C. Protz, B. Bullard, J. Buzzell, C. Garcia, J. Wood, R. Osborne, J. Hulka, and K. G. Cooper, *Additive Manufacturing of Liquid Rocket Engine Combustion Devices: A Summary of Process Developments and Hot-Fire Testing Results*. [Online]. Available: https://arc.aiaa.org/doi/abs/10.2514/6.2018-4625

[4] [Online]. Available: https://www.flickr.com/photos/spacex/16789102495/

[5] "Elon musk tweet." [Online]. Available: https://twitter.com/elonmusk/status/375737311641628672?lang=en

[6] F. Calignano, "Design optimization of supports for overhanging structures in aluminum and titanium alloys by selective laser melting," *Materials & Design*, vol. 64, pp. 203 – 213, 2014. [Online]. Available: http://www.sciencedirect.com/science/article/pii/S0261306914005755

[7] T. Craeghs, S. Clijsters, E. Yasa, F. Bechmann, S. Berumen, and J.-P. Kruth, "Determination of geometrical factors in layerwise laser melting using optical process monitoring," *Optics and Lasers in Engineering*, vol. 49, no. 12, p. 1440–1446, 2011.

[8] Y. Xiong, S. Yao, Z.-L. Zhao, and Y. M. Xie, "A new approach to eliminating enclosed voids in topology optimization for additive manufacturing," *Additive Manufacturing*, vol. 32, p. 101006, 2020. [Online]. Available: http://www.sciencedirect.com/science/article/pii/S2214860419315519

[9] "Lattice optimization analysis." [Online]. Available: https://ansyshelp.ansys.com/account/secured?returnurl=/Views/Secured/corp/v201/en/wb_sim/ds_topo_opt_lattice.html?q=lattice

[10] T. Dbouk, "A review about the engineering design of optimal heat transfer systems using topology optimization," *Applied Thermal Engineering*, vol. 112, p. 841–854, 2017.

[11] M. Pietropaoli, R. Ahlfeld, F. Montomoli, A. Ciani, and M. Dercole, "Design for additive manufacturing: Internal channel optimization," *Journal of Engineering for Gas Turbines and Power*, vol. 139, no. 10, 2017.

[12] F. wearefathom.com, "Orbex." [Online]. Available: https://orbex.space/vehicle

[13] G. P. Sutton and O. Biblarz, *Rocket propulsion elements*. Wiley., 2017.

[14] M. Leary, M. Mazur, H. Williams, E. Yang, A. Alghamdi, B. Lozanovski, X. Zhang, D. Shidid, L. Farahbod-Sternahl, G. Witt, and et al., "Inconel 625 lattice structures manufactured by selective laser melting (slm): Mechanical properties, deformation and failure modes," *Materials & Design*, vol. 157, p. 179–199, 2018.

[15] E. Musk, "Raptor engine performance," 2000.

[16] P. R. Gradl, "Rapid fabrication techniques for liquid rocket channel wall nozzles," *52nd AIAA/SAE/ASEE Joint Propulsion Conference*, 2016.

[17] P. Gradl, C. Protz, S. Greene, D. Ellis, B. Lerch, and I. Locci, "Development and hot-fire testing of additively manufactured copper combustion chambers for liquid rocket engine applications," 07 2017.

[18] P. Gradl, C. Protz, S. Greene, W. Brandsmeier, K. Morgan, M. Calvert, J. Richard, and D. O'Neil, "Additive manufacturing overview: Propulsion applications, design for, and lessons learned," 12 2017.

[19] M. Thirupathi, N. Madhavi, and K. Simhachalam Naidu, "Design and analysis of a fuel injector of a liquid rocket engine," *International Journal of Engineering and Advanced Technolog*, vol. 4, no. 5, Jun 2015.

[20] P. R. Gradl, C. S. Protz, and T. Wammen, *Additive Manufacturing and Hot-fire Testing of Liquid Rocket Channel Wall Nozzles Using Blown Powder Directed Energy Deposition Inconel 625 and JBK-75 Alloys*. [Online]. Available: https://arc.aiaa.org/doi/abs/10.2514/6.2019-4362

[21] M. Bendsøe, "Bendsoe, m.p.: Optimal shape design as a material distribution problem. structural optimization 1, 193-202," *Structural Optimization*, vol. 1, pp. 193–202, 01 1989.

[22] M. Stolpe and K. Svanberg, "An alternative interpolation scheme for minimum compliance optimization," *Structural and Multidisciplinary Optimization*, vol. 22, pp. 116–124, 09 2001.

[23] C. Mattheck and S. Burkhardt, "A new method of structural shape optimization based on biological growth," *International Journal of Fatigue*, vol. 12, no. 3, pp. 185 – 190, 1990. [Online]. Available: http://www.sciencedirect.com/science/article/pii/014211239090094U

[24] O. Sigmund, "Morphology-based black and white filters for topology optimization," *Structural and Multidisciplinary Optimization*, vol. 33, no. 4, pp. 401–424, Apr 2007. [Online]. Available: https://doi.org/10.1007/s00158-006-0087-x

[25] D. J. Brackett and I. Ashcroft, "Topology optimization for additive manufacturing," 2011.

[26] M. Langelaar, "An additive manufacturing filter for topology optimization of print-ready designs," *Structural and Multidisciplinary Optimization*, 07 2016.

[27] S. Liu, Q. Li, W. Chen, L. Tong, and G. Cheng, "An identification method for enclosed voids restriction in manufacturability design for additive manufacturing structures," *Frontiers of Mechanical Engineering*, vol. 10, no. 2, p. 126–137, 2015.

[28] L. Cheng, P. Zhang, E. Biyikli, J. Bai, J. Robbins, and A. To, "Efficient design optimization of variable-density cellular structures for additive manufacturing: theory and experimental validation," *Rapid Prototyping Journal*, vol. 23, no. 4, p. 660–677, 2017.

[29] L. Cheng, J. Liu, and A. C. To, “Concurrent lattice infill with feature evolution optimization for additive manufactured heat conduction design,” *Structural and Multidisciplinary Optimization*, vol. 58, no. 2, p. 511–535, 2018.

[30] T. S. Boysan, Ulas, “Comparison of different aspect ratio cooling channel designs for a liquid propellant rocket engine,” 2007.

[31] M. Pietropaoli, F. Montomoli, and A. Gaymann, “Three-dimensional fluid topology optimization for heat transfer,” *Structural and Multidisciplinary Optimization*, vol. 59, no. 3, p. 801–812, 2018.

[32] Nicholas Christopher, Thomas Cojocar, Jacob Deery, Ruoqin Jiang, Dawson Kletke, Roman Kobets, Shirley Kong,Stefan Martin, Zachariah Mears, Alexandra Mihaila, Aaron Morrison, Vithusan Rajkumar, Justin Robinson, Kyle Tam, Teresa Tang, and Eumin Yang, “Shark of the sky hybrid rocket,” 2019.

[33] G. V. R. Rao, “Recent developments in rocket nozzle configurations,” *ARS Journal*, vol. 31, no. 11, p. 1488–1494, 1961.

[34] F. Jensen, Ph.D. dissertation, 2018.

[35] R. G. BUDYNAS, *ROARKS FORMULAS FOR STRESS AND STRAIN*. MCGRAW-HILL EDUCATION, 2020.

[36] T. L. Bergman, A. Lavine, and F. P. Incropera, *Fundamentals of heat and mass transfer*. John Wiley & Sons, Inc., 2019.

[37] “In625-0402 powder for additive manufacturing.”

[38] C. Pleass and S. Jothi, “Influence of powder characteristics and additive manufacturing process parameters on the microstructure and mechanical behaviour of inconel 625 fabricated by selective laser melting,” *Additive Manufacturing*, vol. 24, p. 419–431, 2018.

[39] O. Sigmund and K. Maute, “Topology optimization approaches a comparative review,” *Structural and Multidisciplinary Optimization*, vol. 48, 12 2013.

# Appendices

# A. Design Results

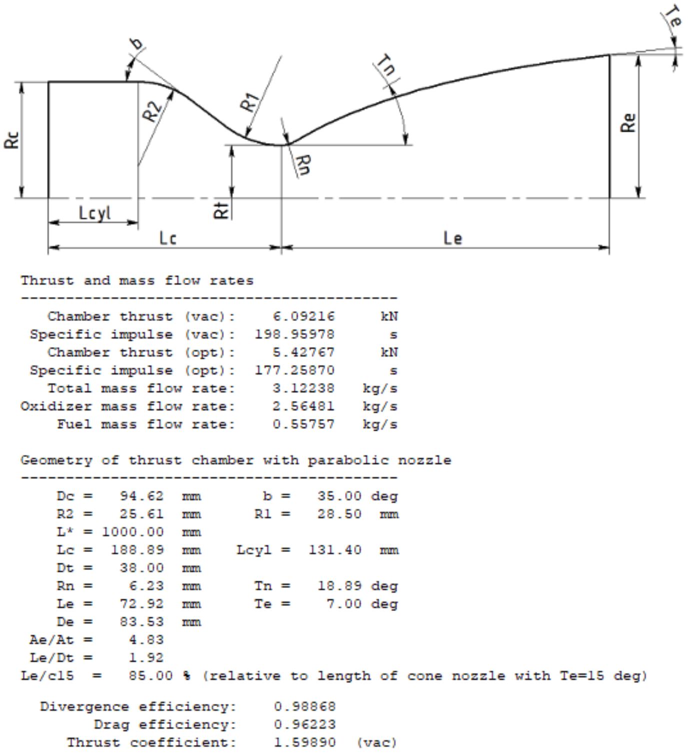

```
Thrust and mass flow rates
------------------------------------------
   Chamber thrust (vac):    6.09216     kN
 Specific impulse (vac):  198.95978      s
   Chamber thrust (opt):    5.42767     kN
 Specific impulse (opt):  177.25870      s
   Total mass flow rate:    3.12238   kg/s
Oxidizer mass flow rate:    2.56481   kg/s
    Fuel mass flow rate:    0.55757   kg/s

Geometry of thrust chamber with parabolic nozzle
------------------------------------------
    Dc =   94.62  mm       b =   35.00 deg
    R2 =   25.61  mm      R1 =   28.50  mm
    L* = 1000.00  mm
    Lc =  188.89  mm    Lcyl =  131.40  mm
    Dt =   38.00  mm
    Rn =    6.23  mm      Tn =   18.89 deg
    Le =   72.92  mm      Te =    7.00 deg
    De =   83.53  mm
 Ae/At =    4.83
 Le/Dt =    1.92
Le/c15  =   85.00 % (relative to length of cone nozzle with Te=15 deg)

  Divergence efficiency:    0.98868
        Drag efficiency:    0.96223
     Thrust coefficient:    1.59890  (vac)
```

**Figure A.1:** Optimized Flow Geometry

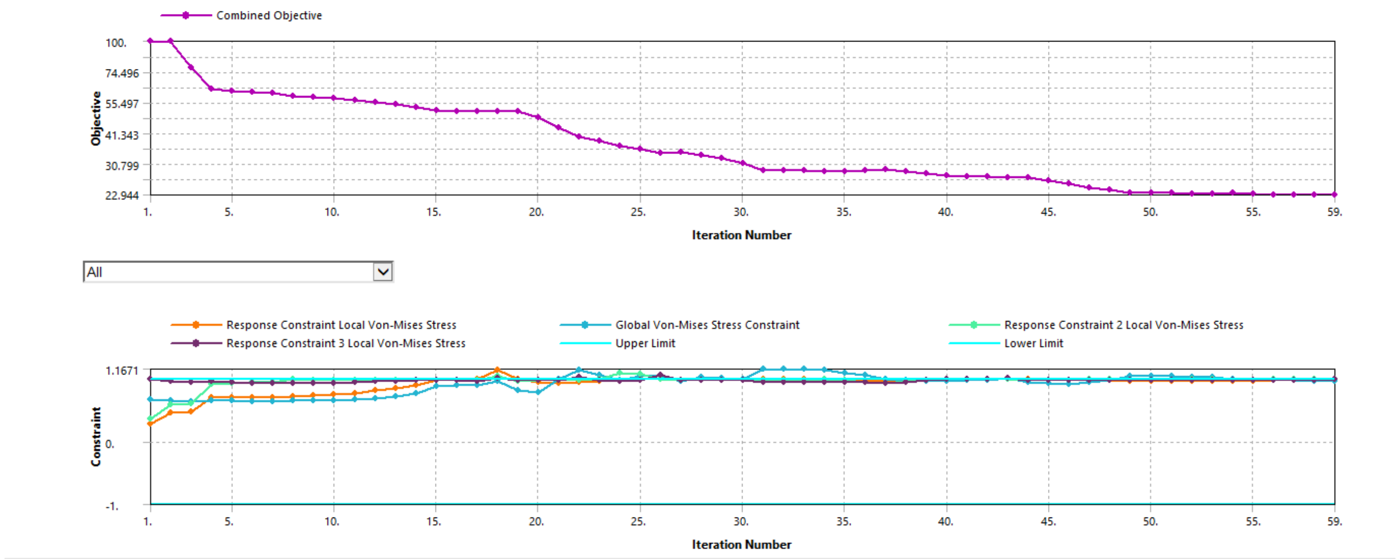

**Figure A.2:** Topology convergence plot for SIMP

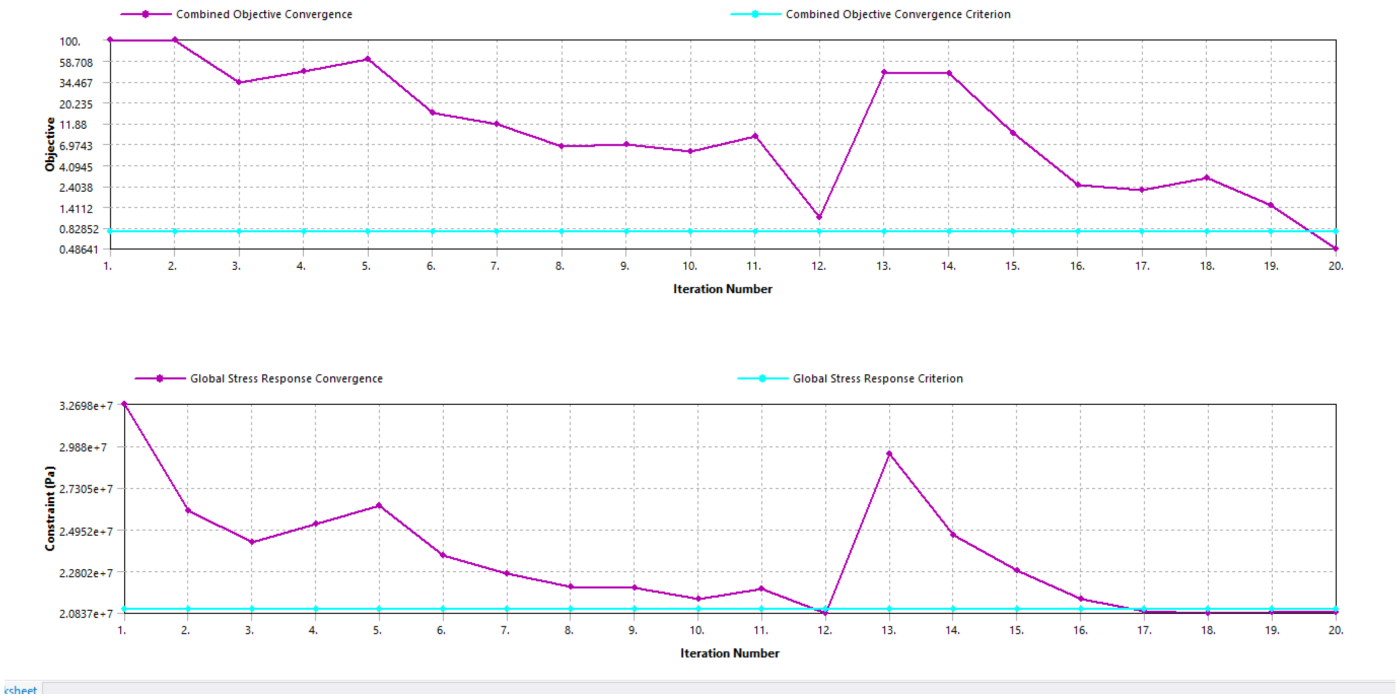

**Figure A.3:** Topology convergence plot for lattice method

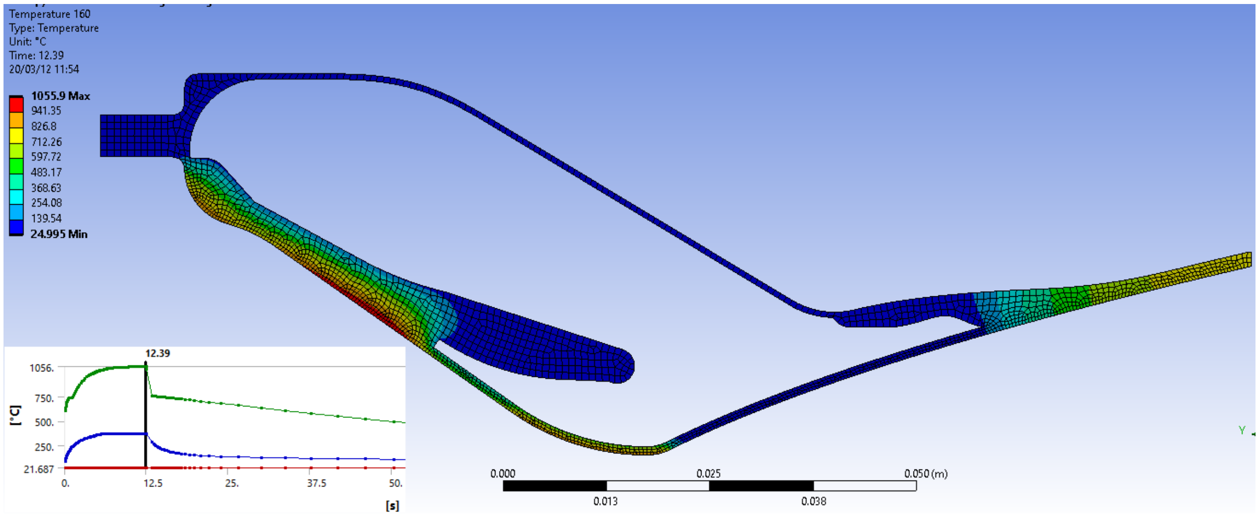

**Figure A.4:** SIMP Design Thermal Performance

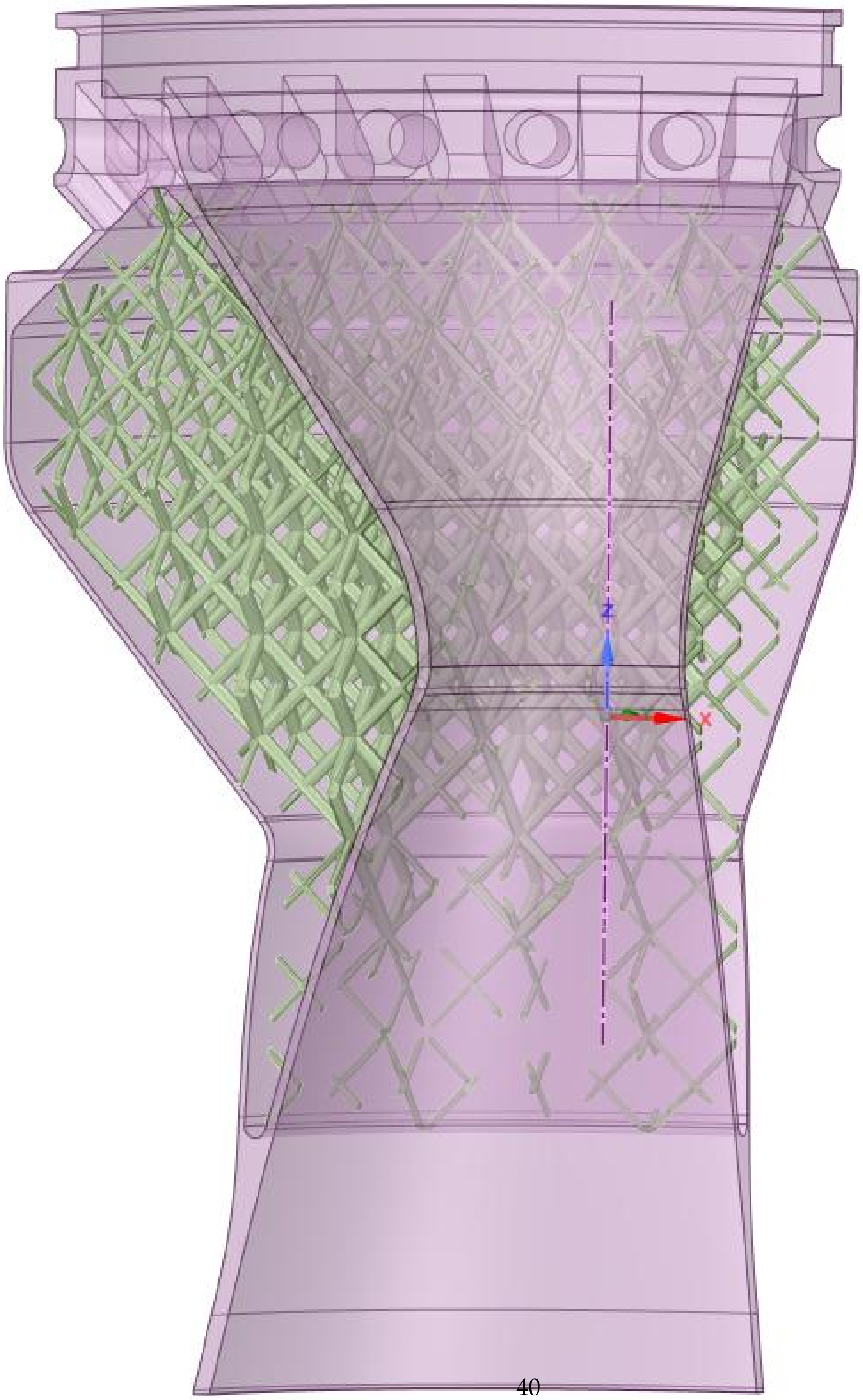

**Figure A.5:** 10mm lattice optimization result

# B. Validation

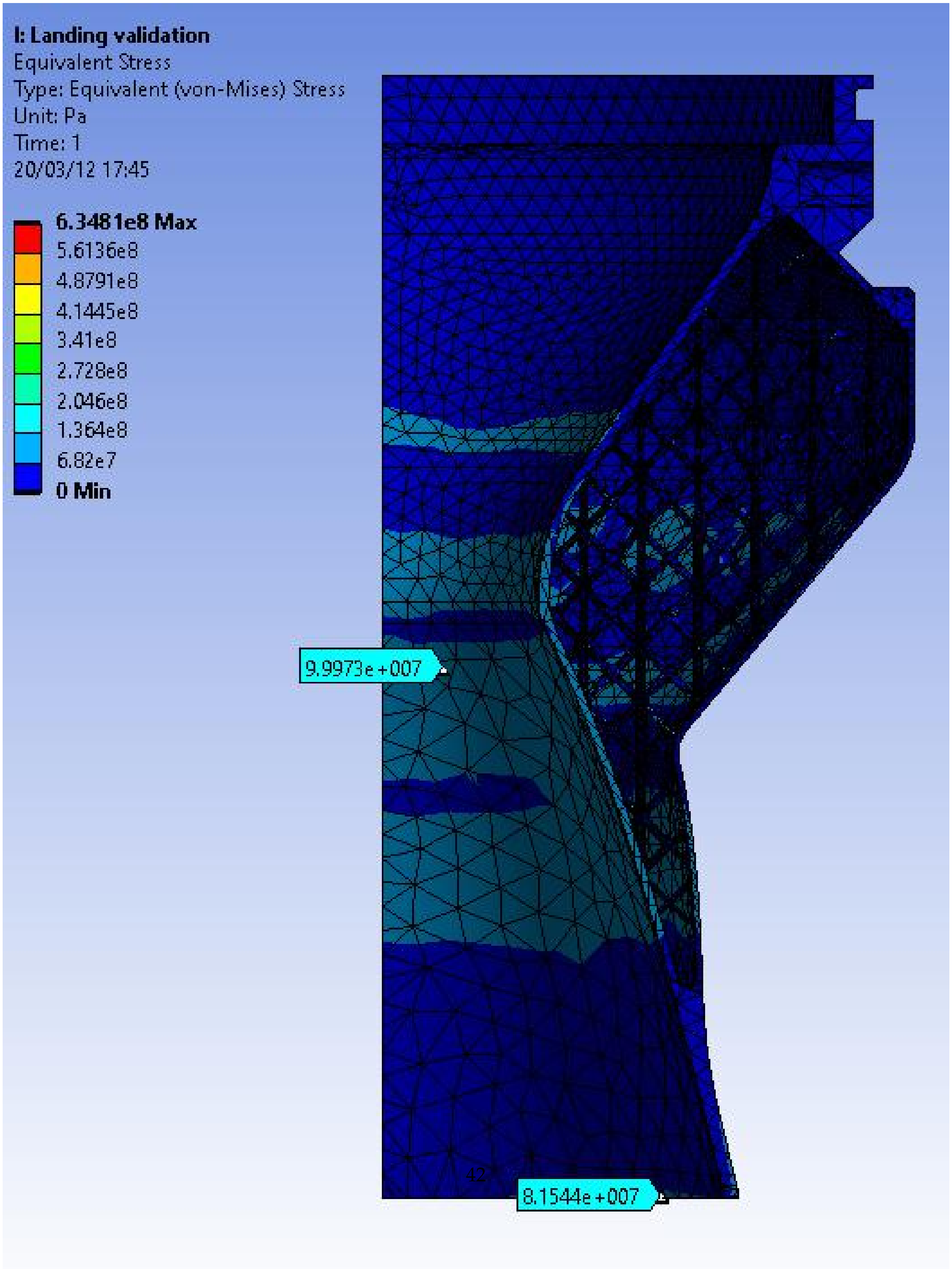

**Figure B.1:** Simulation of 4500N landing force scaled to yield stress

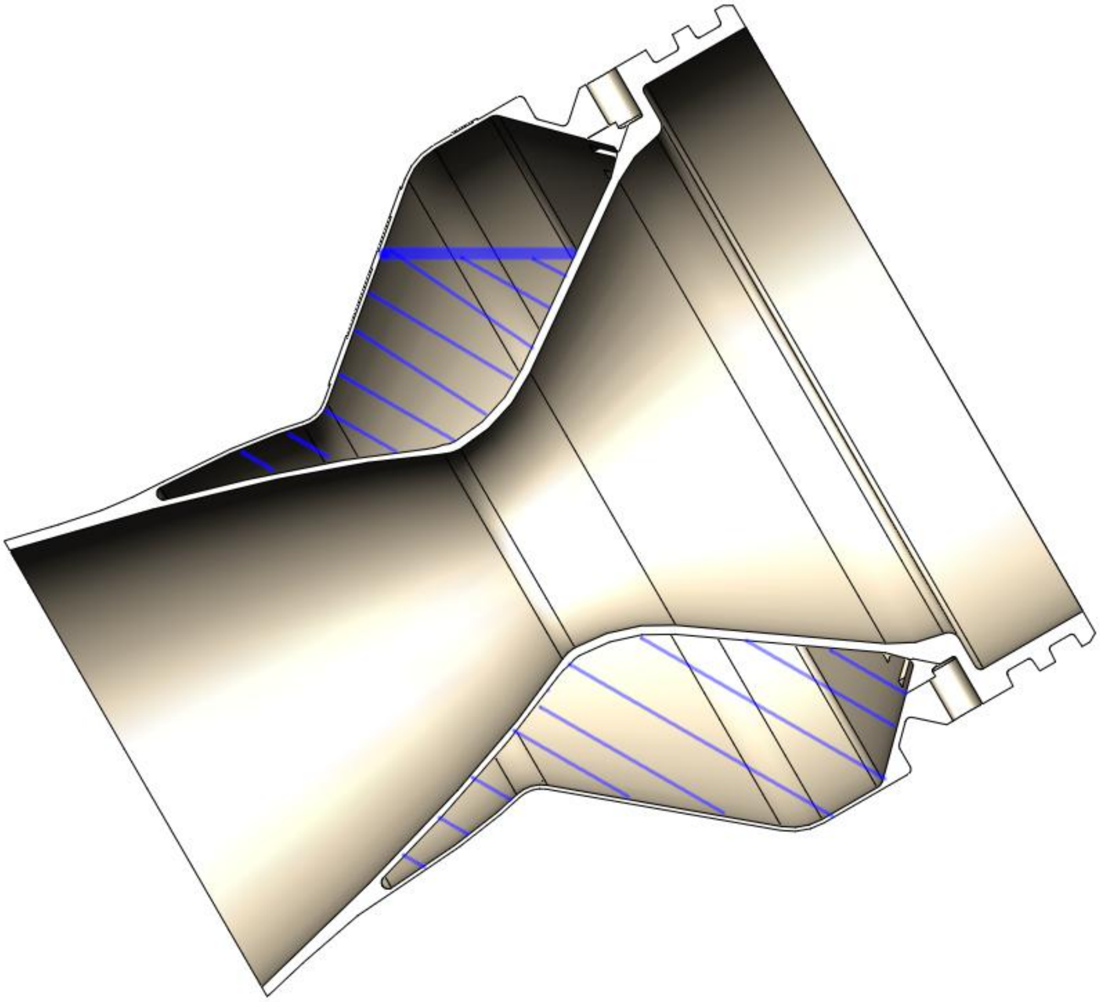

**Figure B.2:** Estimated coolant levels for 30° firing inclination

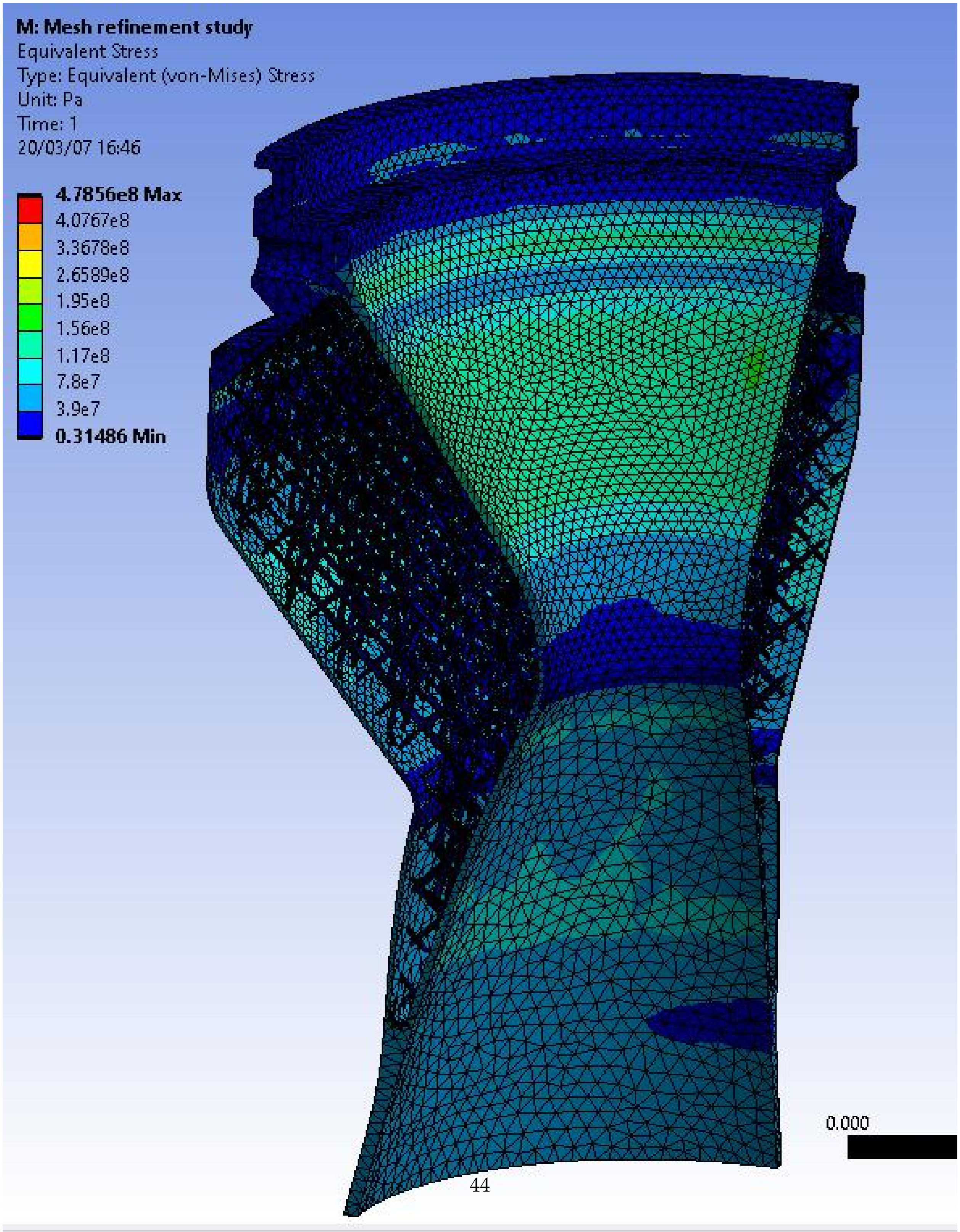

**Figure B.3:** Mesh independence study

# C. Reference Materials

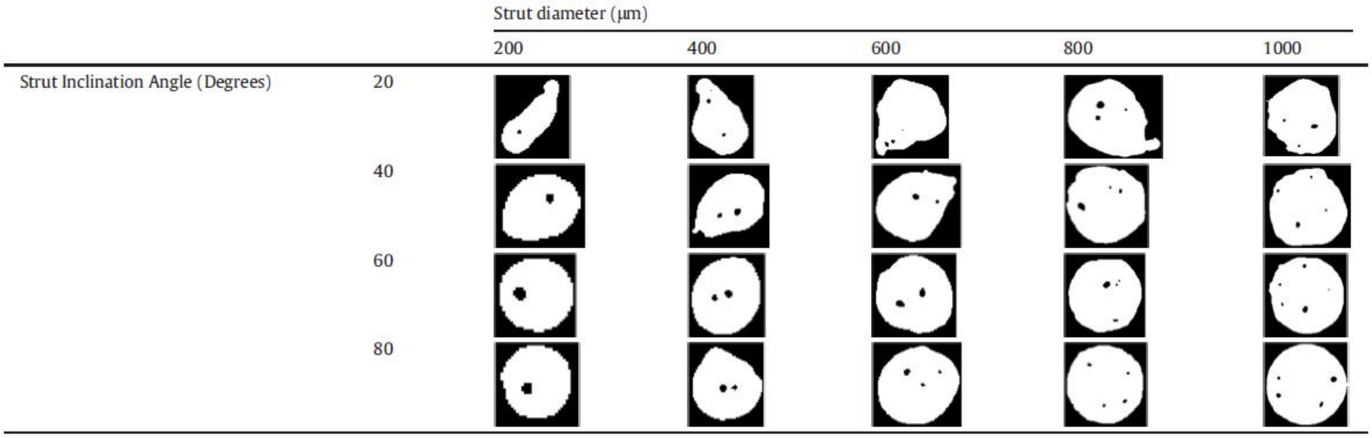

**Figure C.1:** Lattice element porosity for varying print inclinations and feature size from[14]

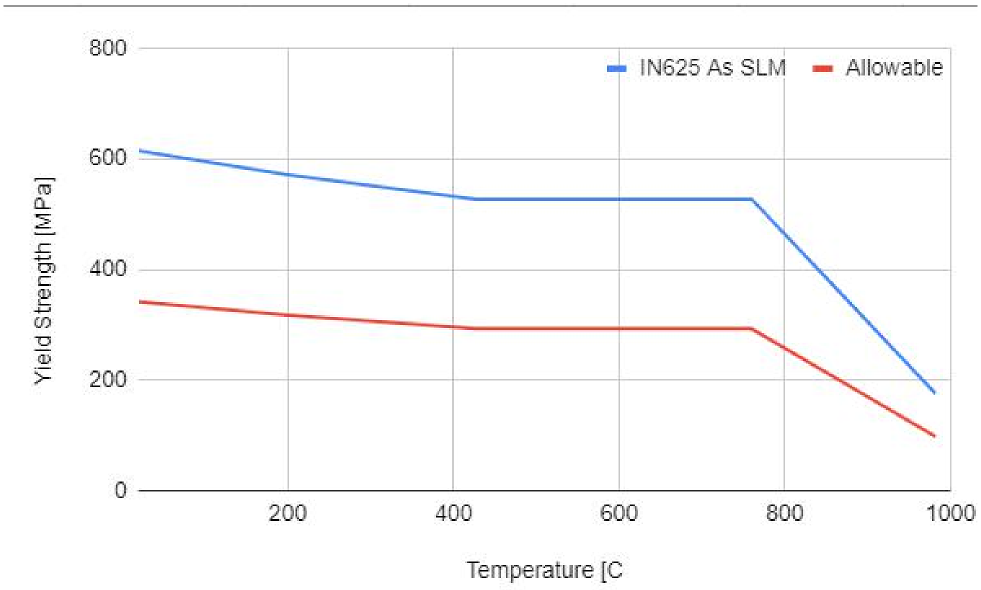

**Figure C.2:** Inconel 625 SLM yield strength (60$\mu$m layer height

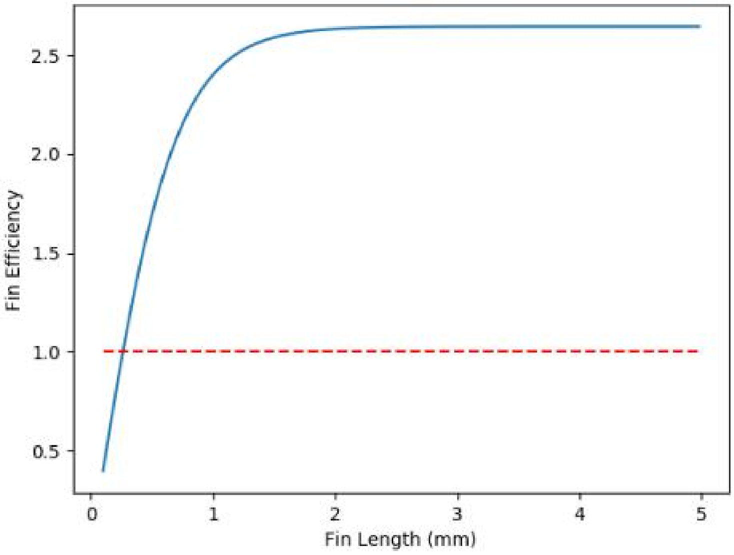

**Figure C.3:** Fin efficiency for Inconel pin fins of ⌀1mm